

Prototype-Aware Multimodal Alignment for Open-Vocabulary Visual Grounding

Jiangnan Xie[†], Xiaolong Zheng^{†*}, Liang Zheng[†]

[†] College of Electronics and Information, Hangzhou Dianzi University, Hangzhou, China

x1zheng@hdu.edu.cn

Abstract

Visual Grounding (VG) aims to utilize given natural language queries to locate specific target objects within images. While current transformer-based approaches demonstrate strong localization performance in standard scene (i.e., scenarios without any novel objects), they exhibit notable limitations in open-vocabulary scene (i.e., both familiar and novel object categories during testing). These limitations primarily stem from three key factors: (1) imperfect alignment between visual and linguistic modalities, (2) insufficient cross-modal feature fusion, and (3) ineffective utilization of semantic prototype information. To overcome these challenges, we present Prototype-Aware Multimodal Learning (PAML), an innovative framework that systematically addresses these issues through several key components: First, we leverage ALBEF to establish robust cross-modal alignment during initial feature encoding. Subsequently, our Visual Discriminative Feature Encoder selectively enhances salient object representations while suppressing irrelevant visual context. The framework then incorporates a novel prototype discovering and inheriting mechanism that extracts and aggregates multi-neighbor semantic prototypes to facilitate open-vocabulary recognition. These enriched features undergo comprehensive multimodal integration through our Multi-stage Decoder before final bounding box regression. Extensive experiments across five benchmark datasets validate our approach, showing competitive performance in standard scene while achieving state-of-the-art results in open-vocabulary scene. Our code is available at <https://github.com/plankXie/PAML>.

1. Introduction

Visual Grounding (VG), also referred to as Phrase Grounding (PG) [24, 77, 21] or Referring Expression comprehension (REC) [84, 42, 85], aims to accurately localize objects described in language expressions within corresponding images, based on a comprehensive understanding of the given image-language query pairs. Given its inherent requirement for deep comprehension of both visual and textual modalities, the effective resolution of VG tasks holds significant potential for application in various other multimodal domains, such as Vision-Language Navigation [1, 74, 47, 87], Visual Question Answering [2, 7, 37, 27], and Human-Robot Interaction [17, 50]. However, most current models are trained using fully supervised learning, which requires access to annotated region bounding boxes and referring expressions. Manually annotating such data in large quantities is extremely costly. Therefore, in recent years, numerous methods have been proposed to alleviate this issue, including semi-supervised learning [91, 29, 58] (where some data is fully annotated and some is partially annotated), weakly supervised learning [59, 70, 5, 12, 65] (where only images and cor-

responding text are provided, without bounding boxes), and unsupervised learning [72, 80, 64, 53, 28] (where only images are given, without any task-related annotations). Additionally, in the complex and diverse real-world scenarios, the objects to be located are often not necessarily encountered during the model's previous training. Consequently, addressing the model's performance in open-vocabulary scenes is more practically significant compared to standard scenes.

Open-vocabulary scenarios, where objects in the test set may not have appeared in the training set, are also referred to as general zero-shot settings in some literature [9]. In recent years, large-scale vision-language pre-training models such as CLIP [49], ALBEF [34], VLMO [3], BLIP [33], CoCa [82], and BEIT-3 [69] have demonstrated robust feature representation capabilities, enabling seamless transfer to downstream tasks [60, 48, 61, 25, 36, 20]. It is natural for us to leverage these powerful models for open-vocabulary visual grounding tasks. However, directly applying these models without fully considering the intrinsic information within the image and text can be detrimental to object localization. The TransCP [62] paper innovatively proposes two methods: Context Disentangling and Prototype Discovering and Inheriting [32, 73], which significantly enhance the model's accuracy in both standard and open-vocabulary scenes. Nevertheless, this model only considers intrinsic contextual information and nearest prototype information, making it susceptible to discriminative relational information. When trained on datasets with low-quality context information and complex expressions, such as ReferIt, and tested on other datasets, the model's performance is suboptimal. Additionally, the modal fusion in this model relies solely on simple Hadamard fusion, and other similar Transformer-based methods also perform only superficial modality fusion through simple attention operations on dual-modal data. Therefore, more thorough modality fusion is critically necessary.

Based on a comprehensive analysis of the strengths and limitations of prior works, we propose a novel framework PAML designed to enhance model performance in both standard and open-vocabulary scenes. This framework incorporates the ALBEF module, leveraging its robust capabilities in multimodal representation and alignment to derive highly representative and well-aligned image and language features. The Visual Discriminative Feature Encoder can enhance discriminative representations of salient objects while suppressing irrelevant contextual information. Additionally, the framework integrates a Multiple Neighbor Prototype Discovering and Inheriting module, enabling the model to learn from a prototype bank and fully utilize the training data to ground referents in both scenes. Furthermore, a Multi-Stage Decoder module is employed to facilitate modality fusion, thereby promoting the model's localization capabilities across the two scenes.

As illustrated in Fig. 1, the image data is first processed by the ALBEF Visual Encoder to obtain its corresponding embeddings, while the textual data is tokenized and subsequently

*Corresponding Author: Xiaolong Zheng.

fed into the ALBEF Text Encoder with embedded image data for text embedding. These multimodal embeddings are then input into the Visual Discriminative Feature Encoder module to extract highly discriminative visual features. These features are subsequently fed into the prototype bank for the processes of discovering and inheriting, thereby acquiring multiple neighbor visual prototype features. The visual prototype features, along with the visual features unprocessed by the Visual Discriminative Feature Encoder module, are concatenated and combined with the visual query and the linguistic features derived from the ALBEF Text Encoder. This amalgamated data is then input into the Multi-Stage Decoder to facilitate modality fusion. Finally, the visual query is processed by the Prediction Head to obtain the bounding box (BBOX) coordinates of the target object.

In summary, we make five-fold contributions:

- We proposed a novel and effective model, PAML, in which each module collaborates seamlessly. It demonstrates exceptional performance in both standard and open-vocabulary scenarios, achieving SOTA results across multiple benchmark datasets. Extensive ablation experiments are conducted to validate the effectiveness of each individual component.
- We directly utilized a pre-trained ALBEF module for robust encoding and cross-modal alignment.
- Based on the visual context disentangling module in TransCP, we improved it into a Visual Discriminative Feature Encoder by incorporating Laplacian transformation and balancing the contributions of the two transformations through learnable parameters.
- We extend TransCP’s Prototype Discovering and Inheriting by adopting multi-neighbor prototype inheritance instead of nearest-neighbor inheritance, enhancing the richness of prototype representations.
- We proposed a novel Multi-Stage Decoder to address the issue of insufficient modality fusion caused by direct attention operations on dual-modal data in previous Transformer-based methods.

2. Related Work

2.1. Visual Grounding

Existing VG models can be broadly categorized into three types based on multimodal fusion and reasoning paradigms: two-stage methods, one-stage methods, and Transformer-based methods.

Two-stage methods [22, 92, 76, 83, 23, 66] rely on pre-trained object detectors to generate a set of candidate bounding boxes and then measure the similarity between these candidates and the language description to locate the target object. However, this approach is inherently constrained by the performance of the pre-trained detector. If the generated bounding boxes fail to encompass the target object requiring localization, the subsequent network is entirely incapable of accurately determining the object’s position. One-stage methods [78, 68, 39, 56, 77, 8, 38] perform visual-language fusion after embedding the multimodal data and then output the bounding box with the highest score among pre-defined dense anchor points. Nevertheless, the intricate modality fusion modules, coupled with the anchor-based nature of this approach, impose significant limitations on the model’s localization performance.

Transformer-based methods [63, 15, 11, 89, 10, 71, 72, 62] are relatively more elegant. TransVG [15] first leverage Transformers to directly embed and fuse the two modal data, and utilizing a special REG token to directly regress the coordinates of the target object. This model demonstrates commendable performance and has been widely adopted as a baseline in numerous subsequent studies. Zheng et al. [89] proposed the ResVG model, which leverages the Stable Diffusion model to generate a substantial amount of synthetic data, thereby enhancing the model’s comprehension of fine-grained semantics and spatial relationships. Dai et al. [11] introduced the SimVG model, which decouples visual-linguistic feature integration from downstream tasks by employing pre-trained multimodal models and supplementary object tokens. This model integrates a dynamic weight-balancing distillation strategy within a multi-path learning framework to reinforce a lightweight MLP pathway, thereby simplifying the architecture and significantly accelerating inference speed. Xiao et al. [71] introduced the HiVG model, which employs a cross-modal bridge to establish multi-level connections between visual and textual modalities. This approach addresses the inconsistency between visual features and the features required for grounding. Additionally, the model incorporates HiLoRA to adapt cross-modal features from shallow to deep layers, thereby preventing the accumulation of perceptual errors. Transformer-based methods have demonstrated promising performance and are progressively emerging as mainstream approaches in the field of Visual Grounding tasks.

2.2. Zero-Shot Visual Grounding

As previously Sec. 1 mentioned, open-vocabulary is also referred to as general zero-shot settings. Therefore, research on zero-shot related work is enlightening for the study of open-vocabulary visual grounding. ZSGNet [51] summarizes four scenarios for evaluating model performance and introduces a novel dataset for zero-shot visual grounding, establishing itself as a baseline for numerous subsequent studies. Shi et al. [54] proposed leveraging external knowledge to construct a multimodal knowledge graph to address zero-shot visual grounding challenges. With the advancements in pre-trained vision–language models, a series of methods based on such models have emerged in recent years. For instance, Yao et al. [79] introduced CPT, which reformulates visual grounding as a fill-in-the-blank problem with co-referential markers based on color in both images and text, thereby minimizing the gap. The ReCLIP [57] model employs isolated proposals to ingeniously transform the visual grounding problem into an image-text matching task, fully leveraging the capabilities of CLIP. Additionally, it incorporates a spatial relation resolver to address CLIP’s limitations in spatial reasoning. The GroundVLP [52] model utilizes Grad-CAM to highlight regions highly relevant to the language query. Simultaneously, it employs an open-vocabulary object detector to identify all objects consistent with the subject in the expression, ultimately localizing the target object by integrating these two components. The remarkable performance of pre-trained vision-language models in zero-shot visual grounding has inspired us to leverage models such as ALBEF and CLIP to enhance model capabilities in open-vocabulary scene.

3. Methods

We propose PAML, a novel framework designed to effectively address the problem of open-vocabulary scene visual grounding. As illustrated in Fig. 1, the entire network is primarily composed of five key components: (1) ALBEF Encoder, (2) Visual Discriminative Feature Encoder, (3) Multiple Neighbor Prototype Discovering and Inheriting module, (4) Multi-Stage Decoder, and (5)

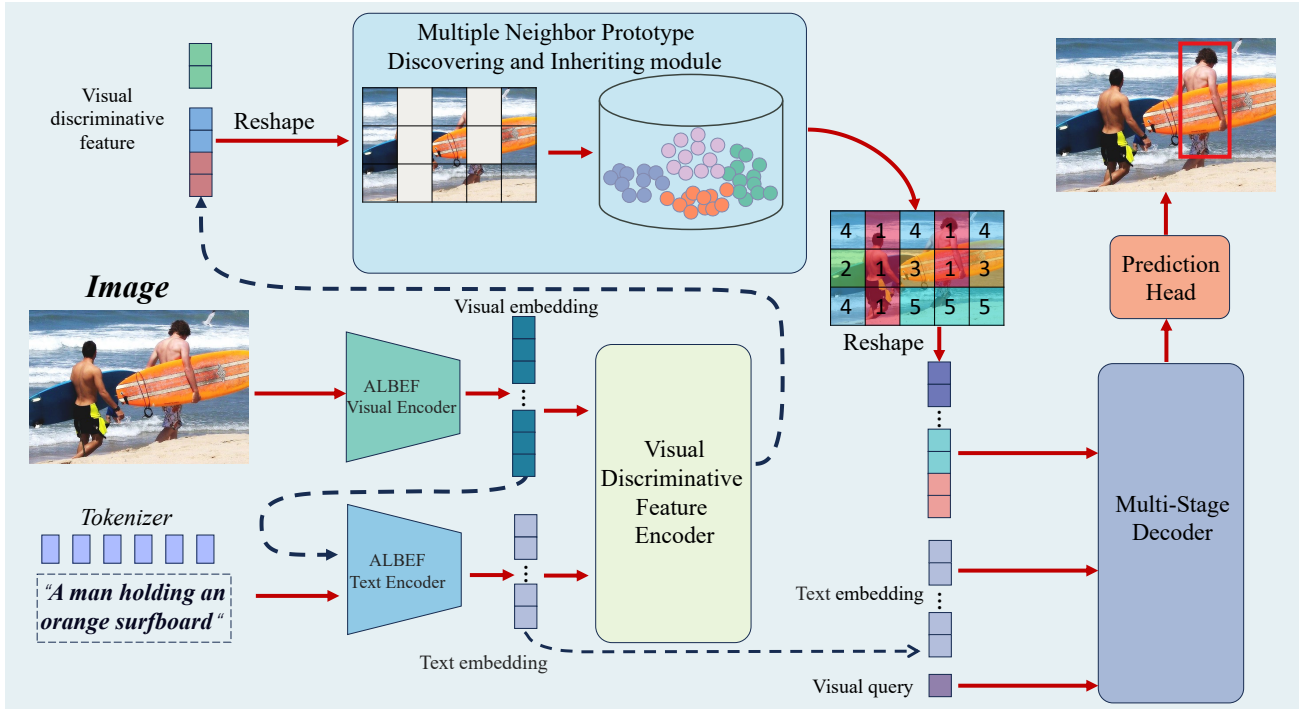


Figure 1: Overall architecture of the proposed PAML. It first aligns image and text features using ALBEF, then enhances object representations while suppressing irrelevant contextual information through Visual Discriminative Feature Encoder. Then it discovers and aggregates multi-neighbor semantic prototypes for open-vocabulary recognition, before fusing multimodal features in a Multi-Stage Decoder. Finally, the REG token is processed by the Prediction Head to regress the coordinates of the target bounding box.

Prediction Head. In the subsequent sections, we will elaborate on the design principles underlying each of these components in detail. The related concepts and definitions of $MHA(\cdot)$, $MCA(\cdot)$, and $MHARPE(\cdot)$ used in the equations can be found in Sec. A.

3.1. ALBEF Encoder

Given a preprocessed image $I \in \mathbb{R}^{B \times 3 \times H_0 \times W_0}$ ($H_0 = W_0 = 256$) and a corresponding text $T \in \mathbb{R}^{B \times L_0}$ ($L_0 = 40$), the image data is initially fed into the ALBEF Visual Encoder. This module primarily adopts a ViT-B/16 architecture. The image undergoes patch embedding processing, transforming it into image tokens with a size of $\mathbb{R}^{B \times 256 \times C_0}$, C_0 is set to 768. These tokens are then concatenated with a learnable class (cls) token $\in \mathbb{R}^{B \times 1 \times C_0}$ initialized to zero. Subsequently, the combined tokens are processed through 12 layers of Transformer Encoder blocks. Following this, the tokens are expanded to 400 via linear interpolation to meet the dimensionality requirements of the subsequent network. Ultimately, image tokens are obtained as the $f_v \in \mathbb{R}^{B \times 400 \times C_0}$.

The input T and f_v are fed into the ALBEF text encoder. Initially, T is passed through the BertEmbeddings module to obtain the preliminary text embeddings $f_{emb} \in \mathbb{R}^{B \times L_0 \times C_0}$. Subsequently, f_{emb} and f_v are input into the BertEncoder module. Within each layer, self-attention operation is performed on the text features, followed by a cross-attention operation between the text and image data. This process is repeated across a total of 12 layers, ultimately yielding $f_l \in \mathbb{R}^{B \times L_0 \times C_0}$ as the final output. In our implementation, we directly employ an off-the-shelf version of ALBEF that has been pre-trained on the MSCOCO dataset. Since we employ the pre-trained ALBEF model, we are able to obtain aligned representations f_l and f_v .

3.2. Visual Discriminative Feature Encoder

Highlighting the features of salient objects in the image while suppressing irrelevant contextual information is crucial for subsequent prototype discovering and inheriting. Therefore, in the second step, f_v and f_l are fed into the visual discriminative feature encoder to obtain the discriminative image features.

Firstly, f_v and f_l undergo linear projection along the feature dimension, with the feature dimension size changing from C_0 to $C = 256$. By utilizing Eq. (1), where f_v is employed as the query and f_l as both the key and value, a MCA operation is performed. This enables us to obtain the linguistic features $f_{linfo} \in \mathbb{R}^{400 \times B \times C}$, which encapsulate information relevant to the objects within the image.

$$f_{linfo} = MCA(f_v, f_l, f_l) \quad (1)$$

Then, a cosine similarity measurement operation is performed between f_{linfo} and f_v to obtain the similarity score $\phi_{sim} \in \mathbb{R}^{400 \times B \times 1}$.

$$\phi_{sim} = \sum_i \left(\frac{f_{linfo(i)}}{\|f_{linfo}\|_2} \cdot \frac{f_v(i)}{\|f_v\|_2} \right) \quad (2)$$

where i is the index over the feature dimensions of the data. Subsequently, Gaussian transformation and Laplacian transformation are applied to ϕ_{sim} to enhance its robustness and expressive capability.

$$\phi_G = \exp\left(-\frac{1 - \phi_{sim}^2}{2\sigma^2}\right) \quad (3)$$

$$\phi_L = \exp\left(-\frac{|1 - \phi_{sim}|}{b}\right) \quad (4)$$

The Gaussian transformation Eq. (3) can smooth ϕ_{sim} , making its data distribution more continuous and stable. This helps mitigate the impact of noise on similarity computation, thereby enhancing the robustness of the model. Additionally, the Gaussian transformation assigns higher weights to values close to 1 (indicating high similarity) while suppressing values far from 1, enabling the model to focus more on highly correlated image regions and text, thus improving the quality of feature fusion. On the other hand, the Laplacian transformation Eq. (4) models the absolute differences in ϕ_{sim} , allowing it to better handle outliers or anomalies, which enhances the stability of the model when dealing with noisy or inaccurate similarity scores. Furthermore,

the Laplacian transformation assigns certain weights to both high and low similarity regions, avoiding the potential issue of the Gaussian transformation overly emphasizing high-similarity areas. Finally, the data from both transformations are combined through a learnable parameter λ (Eq. (5)), which flexibly adjusts the weights of the two transformations to balance the emphasis on high-similarity regions and the robustness to outliers. Initially, λ is set to 0.5.

$$\phi_v = \lambda \phi_G + (1 - \lambda) \phi_L \quad (5)$$

Then, similar to Eq. (1), we employ another MCA layer with different parameters to generate $f_{linfo} \in \mathbb{R}^{400 \times B \times C}$, which represents the guiding information of the text for the image features. Subsequently, the image features are modulated according to Eq. (6).

$$f_{mv} = (f_{linfo} \times \alpha) \times f_v + f_{linfo} \times \beta \quad (6)$$

where $\alpha \in \mathbb{R}^{C \times C}$ and $\beta \in \mathbb{R}^{C \times C}$ are weight parameters, $f_{mv} \in \mathbb{R}^{400 \times B \times C}$ and Eq. (6) integrates the linguistic information into the image features.

$$f_{lcv} = MHARPE(f_{mv}, f_{mv}, f_v) \quad (7)$$

Subsequently, we assign $q = k = f_{mv}$ and $v = f_v$ to execute the MHARPE operation, thereby deriving $f_{lcv} \in \mathbb{R}^{400 \times B \times C}$. This procedure facilitates the incorporation of linguistic information into f_{lcv} , augmenting the representational capacity of the image features, while simultaneously enriching the contextual information of the image and capturing comprehensive global relationships. Finally, Eq. (8) is utilized to generate the discriminative image feature $f_{disv} \in \mathbb{R}^{400 \times B \times C}$. Here, $Norm$ represents $LayerNorm$ with the parameter $\text{eps} = 1e - 5$. we concatenate f_v and f_{disv} in feature dimension and output it to the following modules.

$$f_{disv} = (Norm(f_v) + Norm(f_{lcv})) \times \phi_v \quad (8)$$

While this module shares conceptual similarities with the visual context disentangling module in TransCP, a critical distinction lies in our dual-transformation approach. The TransCP implementation relies solely on Gaussian transformation for feature modulation, which may lead to excessive emphasis on high-similarity regions while aggressively suppressing low-similarity areas. To address this limitation, we introduce a complementary Laplacian transformation that provides more gradual weight distribution, coupled with a learnable parameter λ to dynamically balance their contributions. This synergistic combination, validated through ablation studies in Table 8, demonstrates superior robustness in preserving potentially useful weakly-correlated features while maintaining focus on strongly-aligned regions.

3.3. Multiple Neighbor Prototype Discovering and Inheriting

Prototype information play a crucial role in open-vocabulary scene. However, the Prototype Discovering and Inheriting module in TransCP [62] only considers the nearest tokens to the input. In reality, other proximal prototypes could also contribute to localization to varying degrees. To address this limitation, we have enhanced that module to effectively capture neighboring prototype information within a certain distance threshold of the input token. The obtained f_{disv} is initially upsampled to 768 ($C_1 = 768$) dimensions via a 2D convolutional layer

with both stride and kernel size set to 1, which is denoted as $f_{in} \in \mathbb{R}^{B \times C_1 \times 20 \times 20}$. Subsequently, the data from all batches are aggregated to form the $X \in \mathbb{R}^{(B \times 400) \times C_1}$, which is then fed into the prototype bank module for the processes of discovering and inheriting. The corresponding pseudocode for this procedure is depicted in Algorithm 1.

Algorithm 1 Algorithm of Multiple Neighbor Prototype Discovering and Inheriting

Input: X, E, S, C, k

Output: Q

```

1:  $d_{ij} = \|X_i\|^2 + \|E_j\|^2 - 2 \cdot X_i \cdot E_j^T$ 
2:  $N_i = \text{topk}(-d_{ij}, k)$ 
3:  $w_{ij} = \begin{cases} \frac{\exp(-d_{ij}/\tau)}{\sum_{l \in N_i} \exp(-d_{il}/\tau)} & \text{if } j = N_i \\ 0 & \text{otherwise} \end{cases}$ 
4: if train then
5:    $s_j = \sum_{i=1}^N w_{ij}$ 
6:    $S_j \leftarrow (1 - \alpha) \cdot S_j + \alpha \cdot s_j$ 
7:    $c_j = w_{i,j}^T \cdot X_i$ 
8:    $C_j \leftarrow (1 - \alpha) \cdot C_j + \alpha \cdot c_j$ 
9:    $S \leftarrow \frac{S + \epsilon}{\sum_j S_j + n \cdot \epsilon} \times \sum_j S_j$ 
10:   $E_j \leftarrow \frac{C_j}{S_j}$ 
11: end if
12:  $Q_i = \sum_{j=1}^k w_{ij} E_j$ 
13:  $Q_i \leftarrow \text{sg}(Q_i - X_i) + X_i$ 
14: return  $Q$ 

```

It is essential to initialize the prototype embedding $E \in \mathbb{R}^{2048 \times C_1}$, the cluster size $S \in \mathbb{R}^{2048}$ for each token, and the mean value $C \in \mathbb{R}^{2048 \times C_1}$ of the embeddings for each token within the prototype bank, all of which are set to zero. The squared Euclidean distance between each element of X_i and E_j is computed, followed by obtaining the index $N \in \mathbb{R}^{B \times 400}$ of the nearest k prototype token based on this distance. Subsequently, the index N is transformed into a weight matrix $w \in \mathbb{R}^{(B \times 400) \times 2048}$. the temperature parameter τ is initialized to 1 and made learnable during training. If the process occurs during training, the prototype bank E and its associated statistical quantities are updated. The update procedure begins by calculating the cluster size $s \in \mathbb{R}^{2048}$ for each prototype token E_j (i.e., the number of input data points assigned to this prototype token). The cluster size $S \in \mathbb{R}^{2048}$ is then updated using Exponential Moving Average (EMA). Next, the embedded average $c \in \mathbb{R}^{2048 \times C_1}$ for each prototype token E_j (i.e., the sum of all input data points assigned to this prototype vector) is computed, and the token embedded average C is updated using EMA. The decay rate α is set to 0.4. To prevent the cluster size of certain prototype tokens from being zero, Laplace smoothing is applied to S , and S is used to normalize the prototype tokens, thereby completing the update of E .

Subsequently, the input data is mapped to its nearest k prototype token, yielding the quantized feature $Q \in \mathbb{R}^{(B \times 400) \times C_1}$. Finally, a stop-gradient operation is applied, ensuring that the quantized feature is utilized during forward propagation, while the original input is retained for backward propagation. Experimental results Sec. 4.3.4 demonstrate that the optimal performance is achieved when $k = 5$.

After obtaining Q , it is reshaped into a tensor with the same spatial dimensions as the f_{in} , represented as $f_{qt} \in \mathbb{R}^{B \times C_1 \times 20 \times 20}$. Subsequently, it is concatenated with input along the feature dimension to form a tensor T_{feat} with a size of $\mathbb{R}^{B \times (2 \times C_1) \times 20 \times 20}$. According to Eq. (9), dimensionality reduction and a softmax operation are applied to T_{feat} , yielding T_s .

The $Gate(\cdot)$ is implemented as a 2D convolutional layer with an input channel size of 1, 536, an output channel size of 2, and both stride and kernel size set to 1. The data from the first feature dimension is extracted as $E_s \in \mathbb{R}^{B \times 1 \times 20 \times 20}$, while the data from the second feature dimension is extracted as $I_s \in \mathbb{R}^{B \times 1 \times 20 \times 20}$.

$$T_s = Softmax(Gate(T_{feat})) \quad (9)$$

Finally, prototype out $P \in \mathbb{R}^{B \times C \times 20 \times 20}$ will be obtained through following equation.

$$P = Conv(f_{in} \times I_s + f_{qt} \times E_s) \quad (10)$$

where the $Conv$ is a 2D convolutional layer with an input channel size of 768, an output channel size of 256, and both stride and kernel size set to 1. The feature f_{qt} captures the global structure and semantic information of the input data, effectively representing the distribution of the input data in a high-dimensional space, making it well-suited for tasks with significant inter-class variations. On the other hand, f_{in} preserves the local details and low-level features of the input data, enabling it to capture fine-grained information. Through dynamic weighting mechanisms (I_s and E_s), the model can adaptively integrate global semantic information with local detail information, thereby comprehensively extracting valuable insights from the data. P will be reshaped to a size of $\mathbb{R}^{400 \times B \times 256}$, denoted as f_q .

3.4. Multi-Stage Decoder

In this section, we delve into the intricate workings of the Multi-Stage Decoder. Previous research predominantly employed attention mechanisms to directly fuse modalities among REG tokens, visual tokens, and textual tokens. In contrast, our proposed methodology advocates for a multi-stage approach to modality fusion. The specific procedure is delineated as follows. Initially, a visual query token $f_{vq} \in \mathbb{R}^{1 \times B \times C}$ is initialized as zero, and the T_{info} is computed according to Eq. (11). This involves extracting semantic information pertinent to the visual query from the textual features. Subsequently, the V_{info} is derived using Eq. (12), which entails extracting visual information relevant to the textual query from the image features. Finally, the corresponding visual query is obtained through Eq. (13) and Eq. (14). The Feed-Forward Network (FFN) is composed of two Linear layers with a ReLU activation function in between. The intermediate dimension of the Linear layers is 2,048, while the input and output dimensions of the FFN are both 256.

$$T_{info}^n = Norm(MCA(f_{vq}^{n-1}, f_t, f_t)) \quad (11)$$

$$V_{info}^n = Norm(MCA(T_{info}^n, f_q, f_v)) \quad (12)$$

$$f_{vqt}^n = Norm(f_{vq}^{n-1} + V_{info}^n) \quad (13)$$

$$f_{vq}^n = Norm(f_{vqt}^n + FFN(f_{vqt}^n)) \quad (14)$$

This module design exhibits substantial novelty compared to conventional approaches. Compared to previous approaches in multimodal processing, the extraction of textual and visual information is conducted separately in a decoupled manner. This decoupled design enables the model to handle information from different modalities more flexibly, thereby avoiding direct interference between modalities. Simultaneously, the model leverages a nested attention mechanism, where textual information guides the extraction of visual information, and visual information, in turn, refines the representation of textual information. This nested architecture allows the model to more effectively capture the intricate interactions between modalities.

3.5. Training Objective

The Multi-Stage Decoder consists of a total of 6 layers, and we also utilize the intermediate-layer f_{vq}^i . The corresponding bounding box coordinates are obtained through the Prediction Head, as illustrated in Eq. (15).

$$\hat{B}_i = MLP(f_{vq}^i) \quad (15)$$

The MLP consists of three Linear layers coupled with the Sigmoid activation function. The input and output dimensions of the first two Linear layers are both 256, while the output dimension of the final Linear layer is 4, representing the four coordinates of the bounding box. Following other Transformer-based methods [15] [62], we adopt the $L1$ loss and the GIoU loss as the loss functions during the training phase,

$$\mathcal{L} = \sum_{i=1}^6 (\lambda_{L1} \mathcal{L}_{L1}(B, \hat{B}_i) + \lambda_{GIoU} \mathcal{L}_{GIoU}(B, \hat{B}_i)), \quad (16)$$

where the factors λ_{L1} and λ_{GIoU} are set to 5 and 2 empirically to achieve an optimal balance between the two loss functions. By incorporating the loss corresponding to intermediate queries, the model receives multi-stage supervision during the training process. This multi-stage supervision facilitates improved learning of localization tasks, mitigates the risk of overfitting, and enhances the model's generalization capabilities across diverse scenarios. Additionally, intermediate queries capture feature information at varying scales, which can assist the model in comprehensively understanding the context of the targets, thereby resulting in more accurate localization of those targets.

3.6. Theoretical Analysis

Our framework's effectiveness in open-vocabulary generalization is grounded in fundamental learning theory principles. Below, we provide a detailed theoretical justification for the some key innovations of our approach.

3.6.1 Multi-Prototype Mechanism and Manifold Smoothing

In open-vocabulary scenarios, novel objects often lie in low-density regions of the feature space, where training data is sparse. Previous methods relying on single-prototype matching (e.g., nearest-neighbor retrieval) suffer from high variance in these regions, leading to unstable predictions. Our Multiple Neighbor Prototype Discovering and Inheriting module mitigates this issue by aggregating information from multiple semantically related prototypes. Given a prototype bank $\mathcal{P} = \{p_i\}_{i=1}^M$ and an input feature $\phi(x)$ the inherited prototype feature is computed as:

$$\hat{\phi}(x) = \sum_{k \in \mathcal{N}_K(x)} w_k \cdot p_k \quad (w_k \propto \exp(-\|\phi(x) - p_k\|^2 / \tau)) \quad (17)$$

where $\mathcal{N}_K(x)$ denotes the K-nearest prototypes, and τ is a temperature parameter controlling the sharpness of the weighting. This formulation is motivated by the manifold hypothesis [4], which posits that high-dimensional visual features of semantically similar objects lie near a low-dimensional manifold. When novel object features reside in low-density regions of the manifold (e.g., inter-class boundary zones), single-prototype matching forcibly assigns them to the nearest isolated prototype, thereby disrupting the local topological structure of the manifold. By interpolating between prototypes, our method effectively smooths the decision boundary in regions with limited training data. The generalization error ϵ for novel objects can be decomposed into

bias and variance terms [93]:

$$\mathcal{E} \leq \frac{C}{\sqrt{K}} + L \cdot \mathbb{E} \left[\min_{p \in \mathcal{P}} \|\phi(x) - p\| \right] \quad (18)$$

where C is a data-dependent constant, L is the Lipschitz constant of the downstream predictor. The first term on the right-hand side represents the variance term, while the second corresponds to the bias term. As K increases from 1, the variance term initially dominates - analogous to standard deviation decay in Monte Carlo sampling - causing the error to decrease at a rate of $\mathcal{O}(1/\sqrt{K})$. When K becomes excessively large, the bias term dominates due to the introduction of irrelevant prototypes, leading to increased bias. Our experiments Table 9 show $K = 5$ achieves optimal bias-variance trade-off.

3.6.2 Multi-Stage Fusion as Iterative Refinement

Inspired by the EM algorithm [13], the Multi-Stage Decoder can be decomposed into two steps: (1) Compute cross-modal attention to estimate the relevance between visual regions and language tokens; (2) Update the visual query f_{vq}^n to maximize agreement between modalities. Mathematically, at stage n , the update rule is:

$$f_{vq}^n = \Gamma \left(f_{vq}^{n-1}, \mathcal{F}_{\text{MCA}} \left(f_{vq}^{n-1}, f_l, f_v \right) \right) \quad (19)$$

where Γ is a nonlinear transformation. This iterative process progressively reduces the modal gap $\mathcal{D}_{\text{KL}}(P_{\text{vis}} \| P_{\text{text}})$. The use of intermediate supervision Equation 16 introduces multiple gradient signals during training, which act as a form of implicit regularization. The total gradient is:

$$\nabla_{\theta} \mathcal{L}_{\text{total}} = \sum_{i=1}^6 \lambda_i \nabla_{\theta} \mathcal{L}_i \approx \mathbb{E} [\nabla_{\theta} \mathcal{L}] + \mathcal{O} \left(\sigma / \sqrt{N} \right) \quad (20)$$

where σ is the gradient noise. By averaging over multiple stages, the variance of the gradient estimate is reduced by a factor of $\sqrt{6}$, making optimization more stable and less prone to overfitting.

3.7. Synergy between modules

The PAML framework’s effectiveness stems from a tightly-coupled pipeline where each component’s output strategically feeds into and enhances the next. The ALBEF Encoder’s cross-modal aligned representations serve as the critical foundation, enabling the Visual Discriminative Feature Encoder to perform targeted suppression of irrelevant visual context—this purification process directly optimizes the input for the subsequent prototype discovery stage. The Multiple Neighbor Prototype Discovering and Inheriting module then leverages these noise-reduced features to construct discriminative semantic clusters, with its multi-prototype aggregation mechanism dynamically guided by the linguistic embeddings from ALBEF. These enriched prototypes and the original visual features form complementary streams that the Multi-Stage Decoder intelligently fuses: at each decoding layer, textual semantics steer the attention to relevant prototype features, while the prototypes conversely disambiguate linguistic references through visual evidence. This bidirectional, hierarchical interaction creates a positive feedback loop—where better alignment enables more precise discrimination, which yields higher-quality prototypes, ultimately leading to more accurate fusion and regression. The modules’ interdependence transforms them from isolated processors into an integrated reasoning system that progressively bridges visual and linguistic domains.

4. Experiments

4.1. Datasets

ReferIt. The ReferIt dataset [30], also referred to as ReferItGame or ReferCLEF, comprises approximately 20,000 annotated images sourced from the SAIAPR-12 [19] collection. Each image is associated with one or multiple region-specific referring expressions, though the dataset includes some ambiguous queries (e.g., “any,” “whole”) and occasional labeling errors. Following standard protocols in prior research, the dataset is partitioned into three subsets: a training set with 54,127 expressions, a validation set containing 5,842 expressions, and a test set with 60,103 expressions. The validation set is typically utilized for experimental analysis, while the test set serves as the benchmark for method comparison.

Flickr30K Entities. Flickr30K Entities [46] augments the Flickr30K [81] dataset with short phrase-to-region annotations, comprising 31,783 images annotated with five referring expressions per image, yielding 427K localized phrase-region pairs. The dataset focuses on succinct referential phrases rather than lengthy descriptions and excludes images containing multiple instances of the same object category. Following standard protocols, the data is partitioned into 29,783 training, 1,000 validation, and 1,000 test images.

RefCOCO/ RefCOCO+/ RefCOCOg. Derived from MSCOCO [40], the RefCOCO family comprises three benchmark datasets for referring expression comprehension. RefCOCO [84] contains 19,994 images with 50,000 annotated objects and 142,209 expressions, partitioned into standard splits: training (120,624), validation (10,834), and two test sets - testA (5,657, person-centric) and testB (5,095, object-focused). Its extension, RefCOCO+[84], maintains comparable scale (19,992 images, 49,856 objects, 141,564 expressions) but prohibits spatial descriptors, emphasizing appearance attributes instead. The dataset is officially partitioned into training, validation, testA, and testB subsets containing 120,191, 10,758, 5,726, and 4,889 expressions correspondingly. RefCOCOg [42] expands the collection with 25,799 images and 95,010 expressions, featuring two evaluation protocols: the google split [42] (used in our experiments for consistency with prior work) and the umd split [44].

4.2. Implementation Details

Inputs. The input images are resized to 256×256 resolution, where the longer edge will be resized and the shorter edge will be padded. For referring expressions, we maintain a fixed sequence length of 40 tokens, including special tokens [CLS] and [SEP]. Expressions exceeding 38 tokens are truncated, while shorter sequences are padded with empty tokens after the [SEP] token to maintain consistent dimensionality.

Metric. In line with established evaluation protocols [15, 28, 35], we employ top-1 localization accuracy as our primary metric. A predicted bounding box is deemed correct when its intersection-over-union (IoU) with the ground truth exceeds the conventional threshold of 0.5.

Training Details. We employ the AdamW optimizer to train the model, with the initial learning rate set to $1e - 4$. The ALBEF model, which has a size of 209.5 million parameters, is pretrained on the MSCOCO dataset. The learning rates for the image encoder branch and the text encoder branch of ALBEF are set to $1e - 5$. The learnable parameters σ and b are initialized to 0.5 and 1, respectively. The λ parameter, which balances the contributions of terms ϕ_G and ϕ_L , is initialized to 0.5. All other learnable parameters are initialized using Xavier initialization. The model is trained for 90 epochs across all datasets, with the learn-

Table 1: Comparisons of standard scene with state-of-the-art methods on RefCOCO [84], RefCOCO+ [84] and RefCOCOg [42] in terms of top-1 accuracy (%). We highlight the best and second best performance in the **bold** and underline.

Models	Venue	Backbone	RefCOCO			RefCOCO+			RefCOCOg
			val	testA	testB	val	testA	testB	val-g
Two-stage:									
CMN [23]	CVPR'17	VGG16	-	71.03	65.77	-	54.32	47.76	57.47
VC [88]	CVPR'18	VGG16	-	73.33	67.44	-	58.40	53.18	62.30
ParaAttn [92]	CVPR'18	VGG16	-	75.31	65.52	-	61.34	50.86	58.03
A-ATT [14]	CVPR'18	VGG16	-	80.87	71.55	-	65.13	55.01	63.84
MAttNet [83]	CVPR'18	ResNet-101	76.65	81.14	69.99	65.33	71.62	56.02	-
LGRANs [67]	CVPR'19	VGG16	-	76.60	66.40	-	64.00	53.40	61.78
DGA [76]	ICCV'19	VGG16	-	78.42	65.53	-	69.07	51.99	-
RvG-Tree [22]	TPAMI'19	ResNet-101	75.06	78.61	69.85	63.51	67.45	56.66	-
NMTree [41]	ICCV'19	ResNet-101	76.41	81.21	70.09	66.46	72.02	57.52	64.62
Ref-NMS [6]	AAAI'21	ResNet-101	80.70	84.00	76.04	68.25	73.68	59.42	-
One-stage:									
SSG [8]	arXiv'18	DarkNet-53	-	76.51	67.50	-	62.14	49.27	47.47
FAOA [78]	ICCV'19	DarkNet-53	72.54	74.35	68.50	56.81	60.23	49.60	56.12
RCCF [38]	CVPR'20	DLA-34	-	81.06	71.85	-	70.35	56.32	-
ReSC-Large [77]	ECCV'20	DarkNet-53	77.63	80.45	72.30	63.59	68.36	56.81	63.12
LBYL-Net [26]	CVPR'21	DarkNet-53	79.74	82.71	73.84	68.96	73.52	59.44	63.78
Transformer-based:									
RefTR [35]	NeurIPS'21	ResNet-50	80.92	83.40	75.78	69.22	74.61	60.95	61.76
TransVG [15]	ICCV'21	ResNet-50	80.48	82.57	75.79	66.22	71.25	57.39	67.41
Pseudo-Q [28]	CVPR'22	ResNet-50	56.02	58.25	54.13	38.88	45.06	32.13	49.82
VGTR [18]	ICME'22	ResNet-50	80.48	82.52	75.79	63.46	70.21	53.57	63.76
SeqTR [90]	ECCV'22	DN53	78.22	81.47	73.80	66.01	70.23	55.68	68.26
VLTVG [75]	CVPR'22	ResNet-50	83.21	86.78	78.45	72.36	77.21	64.80	71.40
CLIP-VG [72]	TMM'23	CLIP-B	84.29	87.76	78.43	69.55	77.33	57.62	72.64
TransVG++ [16]	TPAMI'23	ViT-Det	86.28	88.37	<u>80.97</u>	75.39	80.45	66.28	73.86
ScanFormer [55]	CVPR'24	ViLT	83.40	85.86	78.81	72.96	77.57	62.50	74.10
TransCP [62]	TPAMI'24	ResNet-50	84.25	87.38	79.78	73.07	78.05	63.35	72.60
ResVG [89]	ACM MM'24	ResNet-50	85.51	88.76	79.93	73.95	<u>79.53</u>	64.88	73.13
MGCross [43]	TIP'24	ResNet-101	85.10	<u>88.23</u>	80.08	<u>74.44</u>	<u>79.48</u>	<u>65.21</u>	<u>74.50</u>
PAML(Ours)	-	ViT-B/16	<u>85.68</u>	88.07	83.47	72.97	76.70	61.79	74.54

ing rate decaying to $1e-5$ after 60 epochs. according to [75], we set λ_{L1} and λ_{GIoU} to 5 and 2 respectively.

Inference. Following [62], the model is initially trained using standard supervised learning protocols on established benchmarks, with model selection determined by highest validation accuracy. The comprehensive testing procedure encompasses two critical aspects: conventional performance evaluation on standard test sets followed by an analysis of open-vocabulary generalization capabilities. To effectively assess the model's ability to handle novel vocabulary, we implement a systematic cross-dataset evaluation strategy where models trained on ReferIt are tested on RefCOCO series and Flickr30k Entities, those trained on RefCOCO series and Flickr30k Entities, those trained on RefCOCO series are evaluated on ReferIt and Flickr30k, and models developed on Flickr30k are assessed on RefCOCO series and ReferIt. This carefully designed evaluation paradigm perfectly aligns with the fundamental requirements of open-vocabulary scenarios by necessitating generalization to completely unseen datasets containing both familiar and novel object categories.

All model training and inference procedures were executed on a single NVIDIA GeForce RTX 4090.

4.3. Comparisons with State-of-the-art Methods

4.3.1 Comparisons methods

As described in the Related Work, the comparison methods in the experiments can be categorized into three groups:

- Two-stage methods: CMN [23], VC [88], ParaAttn [92], A-ATT [14], MAttNet [83], LGRANs [67], DGA [76], RvG-Tree [22], NMTree [41], Ref-NMS [6], Similarity Net [66], CITE [45], PIRC [31], and DDPN [86].
- One-stage methods: SSG [8], FAOA [78], RCCF [38], ReSC-Large [77], LBYL-Net [26], and ZSGNet [51].

- Transformer-based methods: RefTR [35], TransVG [15], Pseudo-Q [28], VGTR [18], SeqTR [90], VLTVG [75], CLIP-VG [72], TransVG++ [16], ScanFormer [55], TransCP [62], ResVG [89], and MGCross [43].

4.3.2 Comparisons in the Standard Scene

From Table 1, which presents the performance of different models on the RefCOCO series datasets (with the highest accuracy highlighted in **bold** and the second-highest underline), it can be observed that our method demonstrates highly competitive results compared to state-of-the-art (SOTA) approaches. On the RefCOCO validation set, our method achieves an accuracy of 85.68%, which approaches the performance of the best-performing method, TransVG++ 86.28%. Notably, our method achieves an accuracy of 83.47% on the RefCOCO testB dataset, surpassing the second-best method by 2.5%. The performance advantage on testB is particularly significant as it demonstrates our model's robustness in grounding less common or more varied object types compared to person-centric instances. Since the testB dataset exclusively contains non-person objects, this result strongly indicates the superior capability of our model in handling diverse object categories. On the RefCOCOg val-google dataset, our method also achieves state-of-the-art performance with an accuracy of 74.54%. Given that referring expressions in RefCOCOg are generally more verbose and linguistically complex compared to other benchmarks, this result demonstrates our model's superior capability in processing long-form textual descriptions. Transformer-based methods generally outperform both Two-stage and One-stage approaches. For instance, on the RefCOCO dataset, the best-performing Two-stage method, Ref-NMS, demonstrates accuracy deficits of 4.98%, 4.07%, and 7.43% compared to our method on the val, testA, and testB sub-



Figure 2: Qualitative results of our model compared with the TransCP in the standard scene: trained on RefCOCO training set and tested on RefCOCO testA set (first row), and trained on RefCOCOg training set and tested on RefCOCOg val set (bottom row). Green: ground truth; Red: TransCP; Purple: PAML.

Table 2: Comparisons of standard scene with state-of-the-art methods on the test set of ReferIt [30] and Flickr30K Entities [46] in terms of top-1 accuracy (%). We highlight the best and second best performance in the **bold** and underline.

Models	Backbone	ReferIt test	Flickr30K test
Two-stage:			
CMN [23]	VGG16	28.33	-
VC [88]	VGG16	31.13	-
MAttNet [83]	ResNet-101	29.04	-
Similarity Net [66]	ResNet-101	34.54	60.89
CITE [45]	ResNet-101	35.07	61.33
PIRC [31]	ResNet-101	59.13	72.83
DDPN [86]	ResNet-101	63.00	73.30
One-stage:			
SSG [8]	DarkNet-53	54.24	-
ZSGNet [51]	ResNet-50	58.63	63.39
FAOA [78]	DarkNet-53	60.67	68.71
RCCF [38]	DLA-34	63.79	-
ReSC-Large [77]	DarkNet-53	64.60	69.28
LBYL [26]	DarkNet-53	68.14	-
Transformer-based:			
Pseudo-Q [28]	ResNet-50	43.32	60.41
RefTR [35]	ResNet-50	69.04	74.75
VGTR [18]	ResNet-50	63.63	75.44
SeqTR [90]	DarkNet-53	66.97	76.26
VLTVG [75]	ResNet-50	71.41	78.62
TransVG [15]	ResNet-50	69.86	78.07
CLIP-VG [72]	CLIP-B	70.89	81.99
TransVG++ [16]	ViT-Det	73.17	<u>81.49</u>
ScanFormer [55]	ViLT	68.85	-
TransCP [62]	ResNet-50	72.05	80.04
ResVG [89]	ResNet-50	72.35	79.52
MGCross [43]	ResNet-101	<u>75.18</u>	-
PAML(Ours)	ViT-B/16	75.65	79.51

sets, respectively. This indicates that Two-stage methods suffer from significant limitations due to the potential exclusion of target objects during the proposal generation phase. Similarly, on the RefCOCO+ dataset, the top One-stage approach, LBYL-Net, exhibits accuracy gaps of 4.01%, 3.18%, and 2.35% relative to our method. These results suggest that One-stage methods are constrained by their reliance on predefined dense anchor points.

In Table 2, our method achieves state-of-the-art performance on the ReferIt dataset with an accuracy of 75.65%. The ReferIt

dataset presents significant challenges due to its inherent characteristics: multiple referring expressions may describe the same target object (e.g., "red cup" versus "coffee cup"), requiring the model to comprehend synonyms and coreference relationships. Furthermore, the natural language descriptions frequently contain ambiguous expressions (e.g., "that thing"), necessitating effective disambiguation through contextual understanding and visual grounding. The superior performance of our model on this challenging benchmark demonstrates its robustness in handling linguistic variability and referential ambiguity.

To more intuitively demonstrate the advantages of our model, we compare its performance with the TransCP model under standard scene settings. As shown in Fig. 2 (b), (d), (e), and (i), PAML exhibits superior localization capability for small objects. For instance, in Fig. 2 (i), where TransCP fails to localize correctly, PAML accurately identifies the target bus location by leveraging small visual cues ("yellow bars"). Similarly, in Fig. 2 (b), PAML precisely localizes the target based on the small logo ("orca") on clothing. Fig. 2 (c), (f), (g), and (h) further illustrate PAML's ability to localize objects by effectively utilizing attribute-level descriptions. For example, in Fig. 2 (f), PAML correctly identifies the target person with "arms crossed" against a greenish background. In Fig. 2 (g), it successfully localizes the subject matching the textual description ("blue jacket," "jeans," and "brown shoes"). Additionally, Fig. 2 (a) and (j) highlight PAML's robust spatial understanding. Specifically, in Fig. 2 (a), PAML accurately localizes the target head position by reasoning about the relative position of the "glass", whereas TransCP fails under the same condition.

4.3.3 Comparisons in the Open-Vocabulary Scene

Based on the Sec. 4.3.2, it can be concluded that Transformer-based methods exhibit superior performance compared to both Two-stage and One-stage approaches. Therefore, for the sake of conciseness, this chapter will exclusively focus on comparative analyses among Transformer-based methods LBYL-Net [26], RefTR [35], VGTR [18], SeqTR [90], VLTVG [75], TransVG [15], TransCP [62], and ResVG [89]. We conduct experiments under three settings:

- Train on RefCOCO, test on ReferIt and Flickr30K.
- Train on ReferIt, test on RefCOCO series and Flickr30K.

Table 3: Comparison of open-vocabulary scene with the state-of-the-art methods by the models trained on ReferIt and test on RefCOCO/+g and Flickr30K Entities in terms of top-1 accuracy (%). We highlight the best and second best performance in the **bold** and underline.

Models	Flickr30k		RefCOCO			RefCOCO+			RefCOCOg
	val	test	val	testA	testB	val	testA	testB	val-g
LBYL-Net [26]	26.00	26.19	55.61	61.75	46.26	38.03	43.14	29.29	40.02
RefTR [35]	29.88	30.47	58.16	61.15	52.83	36.49	40.15	32.67	44.96
VGTR [18]	14.31	15.01	10.03	7.25	12.91	11.1	7.75	13.60	8.44
SeqTR [90]	17.64	18.38	9.96	9.61	10.13	11.05	9.78	11.82	5.76
VLTVG [75]	51.40	53.13	<u>64.54</u>	<u>65.83</u>	61.98	<u>41.04</u>	<u>43.70</u>	38.33	47.11
TransVG [15]	52.29	54.38	61.67	63.23	59.39	37.52	39.13	35.10	45.79
TransCP [62]	<u>52.92</u>	<u>55.07</u>	64.26	65.55	<u>61.71</u>	40.17	42.70	36.90	<u>47.40</u>
ResVG [89]	52.67	54.71	64.02	65.58	59.99	39.67	41.32	37.03	46.92
PAML(Ours)	53.33	55.63	65.04	67.16	60.1	44.03	47.43	<u>37.96</u>	48.89



Figure 3: Qualitative results of our model compared with the TransCP in the open-vocabulary scene: trained on RefCOCO training set and tested on ReferIt test set(first row), and trained on ReferIt training set and tested on RefCOCO+ testA set (bottom row). Green: ground truth; Red: TransCP; Purple: PAML.

Table 4: Comparison of open-vocabulary scene with the state-of-the-art methods by the models trained on RefCOCO dataset and test on ReferIt and Flickr30K Entities in terms of top-1 accuracy (%). We highlight the best and second best performance in the **bold** and underline.

Models	ReferIt		Flickr30K	
	val	test	val	test
LBYL-Net [26]	21.76	22.93	22.97	21.62
RefTR [35]	27.67	29.45	24.03	23.08
VGTR [18]	23.11	23.46	9.57	9.17
SeqTR [90]	28.78	29.53	15.45	13.97
VLTVG [75]	<u>38.76</u>	40.54	25.28	24.31
TransVG [15]	<u>36.11</u>	37.86	23.78	22.83
TransCP [62]	38.35	<u>40.62</u>	<u>29.01</u>	<u>27.71</u>
ResVG [89]	37.62	39.54	25.77	26.58
PAML(Ours)	41.70	42.78	29.07	27.75

- Train on Flickr30K, test on RefCOCO series and ReferIt.

As shown in Table 4, the proposed approach yields state-of-the-art performance in this experimental configuration, with accuracy scores of 29.07% (val) and 27.75% (test) on Flickr30K, demonstrating a slight but consistent improvement over TransCP(baseline). our method achieves an accuracy of 41.70% on the ReferIt validation set and 42.78% on the test set, surpassing the second-best approach by 2.84% and 2.16%, respectively. These results indicate that the model possesses robust cross-

dataset generalization ability, enabling it to effectively generalize features from the 80 object categories in COCO and adapt them to other datasets with high accuracy.

Table 3 demonstrates that our method delivers exceptional performance in this evaluation setting, achieving state-of-the-art results on all benchmark datasets with the sole exception of the RefCOCO/RefCOCO+ testB subsets. Particularly impressive are the model’s accuracies of 44.03% (val) and 47.43% (testA) on RefCOCO+, which exceed those of the closest competitor by 2.99% and 3.73% respectively. As noted in the Sec. 4.1, the training data in ReferIt dataset comprises substantial amounts of complex and noisy annotations, such as ambiguous referring expressions and mis-labeled regions. These inherent data imperfections present considerable learning difficulties. Remarkably, our approach still establishes new state-of-the-art results, providing compelling evidence for its robustness in real-world scenarios characterized by complex linguistic expressions and imperfect visual grounding annotations.

From Table 5, it can be observed that under this experimental setup, our method still maintains strong performance and achieves the second-highest accuracy on most datasets. For example, on the RefCOCO/RefCOCO+ validation and testA sets, our method attains accuracies of 38.73%, 46.30%, 36.82%, and 42.54%, respectively, trailing the top-performing method by only 0.62%, 0.03%, 0.98%, and 0.37%. However, we note that on the RefCOCO/RefCOCO+ testB sets, our method achieves lower accuracies of 29.87% and 30.70%. This performance gap may stem from the fact that the Flickr30K training dataset primarily

Table 5: Comparison of open-vocabulary scene with the state-of-the-art methods by the models trained on Flickr30K dataset and test on RefCOCO+/g and ReferIt in terms of top-1 accuracy (%). We highlight the best and second best performance in the **bold** and underline.

Models	ReferIt		RefCOCO			RefCOCO+			RefCOCog
	val	test	val	testA	testB	val	testA	testB	val-g
RefTR [35]	36.61	35.70	29.72	36.16	23.21	27.67	31.85	22.21	35.13
VGTR [18]	8.59	8.49	18.33	17.35	11.85	9.09	5.78	11.95	13.05
SeqTR [90]	11.80	11.83	12.41	12.52	11.38	12.70	12.96	11.63	18.44
VLTVG [75]	44.13	42.25	39.67	46.33	31.82	36.28	41.83	<u>31.34</u>	38.63
TransVG [15]	43.07	41.08	36.82	44.67	30.70	35.17	41.97	<u>31.01</u>	44.85
TransCP [62]	<u>45.36</u>	43.99	39.35	46.26	<u>31.76</u>	37.80	42.91	32.95	44.91
ResVG [89]	44.96	42.58	37.01	45.86	30.32	36.71	41.83	30.91	44.62
PAML(Ours)	45.64	<u>43.48</u>	<u>38.73</u>	<u>46.30</u>	29.87	<u>36.82</u>	<u>42.54</u>	30.70	42.09

contains person-centric and common object categories, whereas testB includes more rare or sparse object categories. Consequently, the Multiple Neighbor Prototype Discovering and Inheriting module may fail to learn representative prototype features for these objects, leading to suboptimal localization performance.

For a more intuitive demonstration of our model’s advantages, we compare its performance with the baseline TransCP model under open-vocabulary settings in Fig. 3. Fig. 3 (a), (d), and (g) demonstrate PAML’s robust localization capability even when provided with only a single-word query. This scenario requires precise and comprehensive semantic understanding of the isolated term. For instance, in Fig. 3 (d), the model accurately localizes the “building” while producing more reasonable results than the ground truth annotation. Fig. 3 (e), (b), and (j) highlight PAML’s superior performance in small-object localization. Notably, in Fig. 3 (j), the model successfully localizes the challenging target “blue shirt arm” where TransCP completely fails. Furthermore, Fig. 3 (i) showcases PAML’s exceptional ability to interpret and localize human actions, as evidenced by its accurate detection of the “texting” behavior.

4.3.4 Ablation Study

In this section, we will present a comprehensive validation of the contribution of each module within the model to the overall experimental outcomes. Table 6 and Table 7 present the ablation study results in the standard-scene and open-vocabulary scene, respectively. AL, VD, PT, and MD denote the ALBEF Encoder, Visual Discriminative Feature Encoder, Multiple Neighbor Prototype Discovering and Inheriting module, and Multi-Stage Decoder, respectively. A checkmark (✓) indicates module usage, while a blank entry denotes its exclusion. Without employing ALBEF, we substitute both the image encoder and text encoder with pre-trained models of comparable scale: ViT-B/16 (85.8M parameters) for visual processing and BERT-base (123.7M parameters) for textual processing. Generally, the experimental results demonstrate that the model’s accuracy declines when any individual module is omitted.

In Table 6, we observe that employing only the Multi-Stage Decoder (MD) yields the most significant performance improvement in the standard-scene compared to using either of the other two modules alone. For instance, on the RefCOCO val, testA, and testB datasets, adding only MD improves performance by 3.1%, 3.05%, and 5.66%, respectively, compared to the baseline without any of these modules.

The performance improvement can be attributed to our Multi-Stage Decoder architecture, which effectively captures fine-grained semantic relationships between extended linguistic expressions and visual features through iterative cross-modal fusion. Furthermore, the results indicate that employing the Multiple Neighbor Prototype Discovering and Inheriting module (PT) alone yields marginal performance gains. For instance, on the

RefCOCO+ dataset, integrating only PT improves accuracy by merely 0.23%, 0.07%, and 0.04% across different splits compared to the baseline configuration. However, a substantial performance boost is observed when PT is combined with the Visual Discriminative Feature Encoder (VD). On the ReferIt test set, the joint use of VD and PT achieves a 2.2% accuracy improvement, significantly surpassing the individual contributions of VD (0.9%) and PT (0.09%). This suggests that the prototype discovery and inheritance mechanism effectively functions when paired with a Visual Discriminative feature encoder that can first highlight target objects while suppressing irrelevant contextual information. Furthermore, a performance gap of 1.74% in accuracy is also observed between ALBEF and the baseline model using separate ViT-B/16 and BERT-base encoders on the ReferIt test dataset. It can be primarily attributed to ALBEF’s superior multimodal fusion architecture and training paradigm, which enables more effective cross-modal alignment through its integrated cross-attention mechanisms and contrastive learning objectives, as opposed to the late fusion approach of separately pre-trained unimodal encoders that may suffer from representation incompatibility and insufficient fine-grained visual-textual correspondence optimization.

Similar observations can be drawn from Table 7. Notably, on the ReferIt test set, the VD+PT module combination achieves 1.03% higher accuracy than VD+MD. However, the opposite trend is observed in Table 6 (standard-scene setting). This indicates that the PT module effectively captures and transfers object-level prototype information across datasets, thereby enhancing localization performance. In contrast, since standard scenes do not involve cross-category discrepancies between training and test sets, the performance gain from prototype transfer is less pronounced.

Eq. (3), Eq. (4) and Eq. (5) describe the process where input ϕ_{sim} undergoes both Gaussian and Laplacian transformations, with the resulting outputs being combined via learnable weighting parameters λ to produce ϕ_v . The effectiveness of this operation is also verified through ablation experiments, with corresponding results shown in Table 8. When the learnable parameter λ is disabled, we simply average inputs ϕ_G and ϕ_L with fixed weights of 0.5. As shown in Table 8, the model achieves its poorest performance (84.91%, 87.51%, and 82.64% across different sets) when either transformation is omitted. The introduction of either Gaussian or Laplacian transformation yields consistent improvements - for instance, employing just the Gaussian transform boosts performance by 0.36%, 0.3%, and 0.2% respectively. However, when both transformations are applied without the learnable parameter λ , the accuracy remains suboptimal, trailing the full configuration by 0.36%, 0.17%, and 0.18%. These results substantiate two key findings: first, both transformations are essential for smoothing the data distribution ϕ_{sim} to reduce noise sensitivity and enhance robustness; second, the

Table 6: Ablation study of different modules in standard scene.

Modules				ReferIt test	RefCOCO			RefCOCO+		
AL	VD	PT	MD		val	testA	testB	val	testA	testB
✓				72.52	80.99	82.97	76.32	66.71	72.25	57.49
✓	✓			73.42	82.73	85.07	77.23	68.42	74.85	58.31
✓		✓		72.61	81.02	83.02	76.41	66.93	72.32	57.53
✓			✓	74.53	84.09	86.02	81.98	70.99	75.45	60.09
✓		✓	✓	74.87	84.42	86.75	82.27	71.33	75.78	60.21
✓	✓		✓	75.49	85.51	87.86	83.19	72.68	76.64	61.53
✓	✓	✓		74.72	85.01	86.21	83.02	72.13	76.28	61.44
✓	✓	✓	✓	73.91	84.93	86.63	82.87	71.84	75.73	60.97
✓	✓	✓	✓	75.65	85.68	88.07	83.47	72.97	76.70	61.79

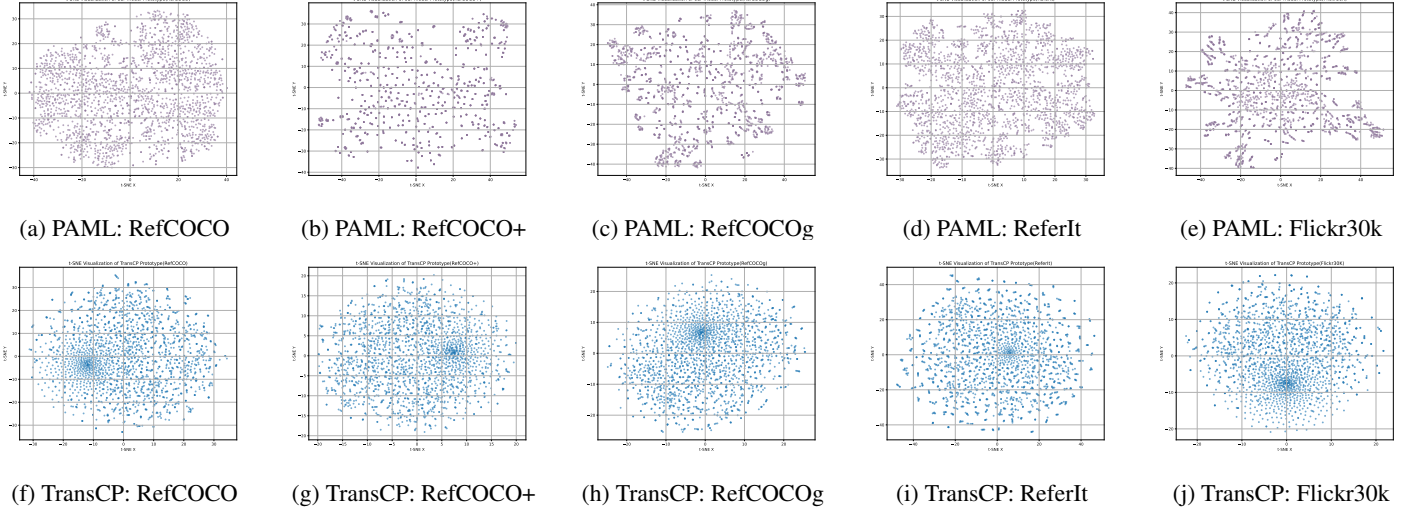


Figure 4: A t-SNE visualization is presented to compare the prototype bank distributions between our PAML framework (top row) and the TransCP baseline (bottom row) across five benchmark datasets (left to right: RefCOCO, RefCOCO+, RefCOCOg, ReferIt, and Flickr30K).

Table 7: Ablation study of different modules in open-vocabulary scene, trained on RefCOCO and test on ReferIt.

Modules			ReferIt	
VD	PT	MD	val	test
			36.71	38.44
✓			37.42	39.21
	✓		36.94	38.51
		✓	38.04	39.55
	✓	✓	38.51	40.07
✓		✓	40.28	40.67
✓	✓		41.31	42.29
✓	✓	✓	41.70	42.78

Table 8: Ablation study of different transformations in standard scene.

Modules			RefCOCO		
gaussian	laplacian	λ	val	testA	testB
			84.91	87.51	82.64
✓			85.27	87.73	82.84
	✓		85.21	87.81	82.90
✓	✓		85.32	87.90	83.29
✓	✓	✓	85.68	88.07	83.47

learnable parameter λ is crucial for optimally balancing the complementary strengths of these transformations in the final output. As mentioned in Sec. 3.2, The Gaussian transformation empha-

Table 9: Ablation study of different number of neighbor prototypes in standard scene

Prototype	RefCOCO		
	val	testA	testB
1	84.31	87.42	80.02
3	85.16	87.61	82.89
5	85.68	88.07	83.47
7	85.49	87.82	82.95
9	84.60	87.31	81.57

sizes values near 1, which correspond to strong similarities, by assigning them higher weights, thereby allowing the model to concentrate more on regions with high correlation between images and text. This helps improve the effectiveness of feature merging. Conversely, the Laplacian transformation captures the absolute differences in ϕ_{sim} , making it more adept at managing outliers or anomalies. This results in increased stability, especially when the similarity scores are noisy or unreliable. Additionally, unlike the Gaussian approach, the Laplacian method distributes weights across both high and low similarity regions, preventing the model from disproportionately focusing only on highly similar areas. Consequently, maintaining an equilibrium between the contributions of both transformations is crucial for model performance.

Our Multiple Neighbor Prototype Discovering and Inheriting module computes the input feature’s corresponding prototype via a distance-based weighted summation of its 5 nearest prototypes. To analyze the effect of the number of prototypes

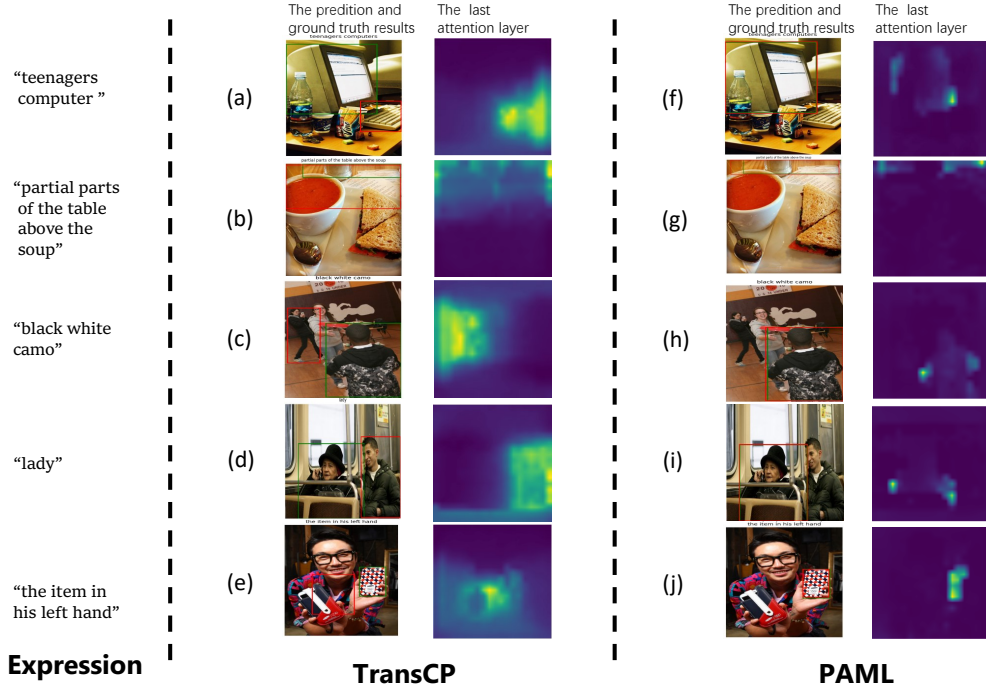


Figure 5: presents a comparative visualization of prediction results and final-layer attention maps between PAML (right column) and TransCP (middle column), with corresponding expressions for each example(left column) in the standard scene that train on RefCOCO training set and test on RefCOCO testA set. Red: prediction result; Green: ground truth.

involved in this operation, we conduct ablation experiments using 1, 3, 5, 7, and 9 prototypes. The model’s performance on the RefCOCO benchmark under standard-scene settings is reported in Table 9. The experimental results demonstrate that incorporating the 5 nearest prototypes achieves the best performance, while deviations—either reducing or increasing the number of prototypes—adversely affect model accuracy. For instance, when only 1 nearest prototype is considered, the model exhibits performance declines of 1.37%, 0.65%, and 3.45% on the val, testA, and testB splits, respectively, relative to the 5-prototype configuration. Conversely, expanding the prototype count to 9 leads to reductions of 1.08%, 0.76%, and 1.90% in accuracy across the same evaluation sets. The experimental results demonstrate that relying solely on a single prototype may fail to comprehensively capture the diversity of input features, particularly when the input lies in the semantic boundary regions between multiple prototypes. Such single-prototype inheritance can lead to information loss. The distance-weighted mechanism enables the model to dynamically adjust the contribution of each prototype, thereby achieving more precise fitting of the input feature distribution. For instance, local details may be predominantly captured by nearby prototypes, while the global structure is jointly characterized through the collaborative representation of multiple prototypes. However, The inclusion of an excessive number of prototypes risks introducing irrelevant feature representations into the weighted aggregation, thereby compromising model accuracy. Consequently, determining an optimal number of nearest-neighbor prototypes is critical for maintaining performance as well.

To analyze the computational complexity of PAML, we conduct experiments to determine time cost during both training and inference phases. The computational efficiency analysis measures training latency by averaging the execution time across 10 stochastic forward-backward passes, while inference performance is evaluated solely through forward propagation timing. All comparative models (TransVG, TransCP, and PAML) were implemented on an NVIDIA GeForce RTX 4090 GPU with

Table 10: Comparison of the time cost and parameters with the baselines on the test split of ReferIt dataset.

Models	Params. (M)	Training (ms)	Inference (ms)
TransVG	150.96	122.79	37.22
TransCP	160.43	119.59	39.89
PAML	163.57	123.37	41.25

24GB memory under identical experimental conditions (batch size = 1), using ReferIt test split as the evaluation benchmark, with quantitative results presented in Table 10. Our analysis reveals that although PAML exhibits moderately increased parameter counts (+2%), training time (+3.2%), and inference time (+3.4%) compared to TransCP, these computational overheads remain within the same order of magnitude. Crucially, PAML delivers superior cost-effectiveness when considering its performance gains - achieving 5% higher accuracy on the ReferIt test benchmark than TransCP. This evidence strongly suggests that the novel methods (e.g., multi-prototype mechanism, multi-stage fusion) introduce only marginal computational complexity while significantly enhancing model capability.

4.4. Visualization

4.4.1 Prototype Bank

For a more comprehensive understanding of the prototype bank’s underlying mechanism, we visualize the prototype banks of our model and the TransCP model, both trained on five distinct datasets, by applying t-SNE to reduce their dimensionality from 2048×768 to 2048×2 . The resulting 2D projections are shown in Fig. 4. As shown in the Fig. 4, although we predefined the prototype bank size as 2048, the actual number of points projected onto the 2D plane is significantly fewer than 2048. This indicates that some prototype features gradually converge in the semantic space during training and can ultimately be considered as identical prototypes. This aligns with our expectations, since the actual number of distinct prototypes within the dataset is neces-

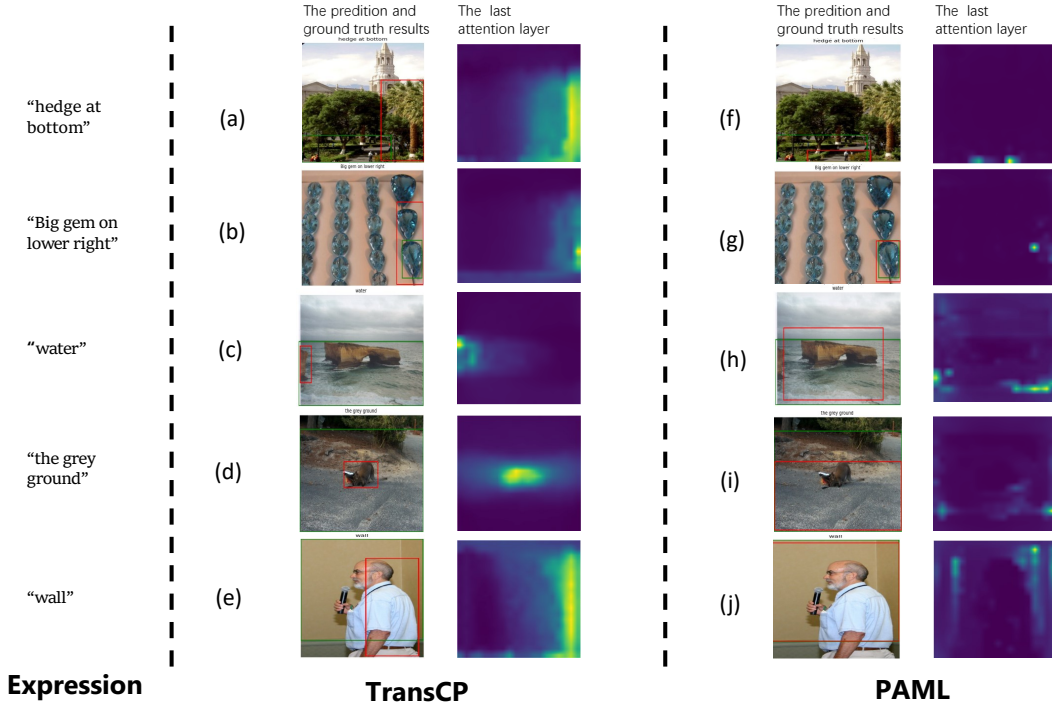


Figure 6: presents a comparative visualization of prediction results and final-layer attention maps between PAML (right column) and TransCP (middle column), with corresponding expressions for each example (left column) in the open-vocabulary scene that train on RefCOCO training set and test on ReferIt val set. Red: prediction result; Green: ground truth.

sarily smaller than the predefined bank size of 2048. The number of prototypes is closely related to the training dataset characteristics. For instance, the ReferIt dataset typically contains images with numerous targets and descriptions involving complex spatial relationships, whereas Flickr30K primarily consists of humans and common object categories. Consequently, ReferIt theoretically requires more prototypes. Fig. 4c and Fig. 4e demonstrate that the prototype bank trained on ReferIt exhibits a more dispersed distribution compared to that trained on Flickr30K, representing a greater number of distinct prototypes, which aligns with our theoretical analysis. Furthermore, the prototype distributions demonstrate higher density in our approach relative to TransCP, suggesting more effective prototype representation learning. This characteristic fundamentally accounts for our method’s performance advantages in open-vocabulary scene.

4.4.2 Attention map

To further highlight the strengths of our proposed model, we generate attention map visualizations of the attention scores corresponding to the [REG] tokens in the final attention layer, comparing our approach with the TransCP model. We select representative examples from both the standard-scene and open-vocabulary scene settings, which are subsequently visualized in Fig. 5 and Fig. 6, respectively. All images and referring expressions in Fig. 5 are sampled from the RefCOCO dataset (val, testA, and testB splits), while the model was exclusively trained on the RefCOCO train split. For Fig. 6, the visual-grounding pairs originate from the ReferIt dataset (val and test splits), though the model maintains the same training protocol using only RefCOCO training data.

As demonstrated in Fig. 5(a), (f), (d), (i), and Fig. 6(c), (h), (e), (j), our model exhibits superior fine-grained word comprehension compared to TransCP. For instance, it accurately localizes regions corresponding to specific words such as “lady” (identifying females in images) and “water” (detecting aqueous regions).

Furthermore, Fig. 5(b), (g), (e), (j) and Fig. 6(a), (f), (b), (g) highlight our model’s enhanced spatial reasoning capabilities. Notably, the localization task in Fig. 3(e), (j) is particularly challenging, as it requires interpreting object positions from the human perspective (e.g., held items) rather than the image’s global viewpoint. Our model’s precise predictions in these cases underscore its robust understanding of linguistically specified spatial relationships.

Additionally, Fig. 5(c), (h) and Fig. 6(d), (i) reveal our model’s improved semantic accuracy for domain-specific vocabulary. For example, given the phrase “black white camo”, TransCP erroneously associates it with a “female in black clothing holding a white phone”, failing to capture the true meaning (camouflage pattern). In contrast, our model correctly interprets the term and localizes the target object.

Meanwhile, Regarding the attention maps, we observe that, compared to TransCP, our model generates attention maps that are more focused on specific regions and already exhibit approximate contours of the target objects, achieving a segmentation-like effect. This indicates a unique advantage of our model in the task of target localization.

4.4.3 Irrelevant context suppression

In Sec. 3.2, we introduced that the Visual Discriminative Feature Encoder enhances salient objects while suppressing irrelevant contextual information. To verify this functionality, we extract attention weights from both the final attention layer preceding this module (i.e., the last layer of ALBEF’s Visual Encoder) and the final attention layer within the Visual Discriminative Feature Encoder, visualizing them as attention maps in Fig. 7 for comparative analysis. From the attention maps, we can observe that before applying the Visual Discriminative Feature Encoder, the attention weights are diffusely distributed, whereas after processing through the Visual Discriminative Feature Encoder, the model successfully highlights language-relevant objects in the image while significantly suppressing irrelevant en-

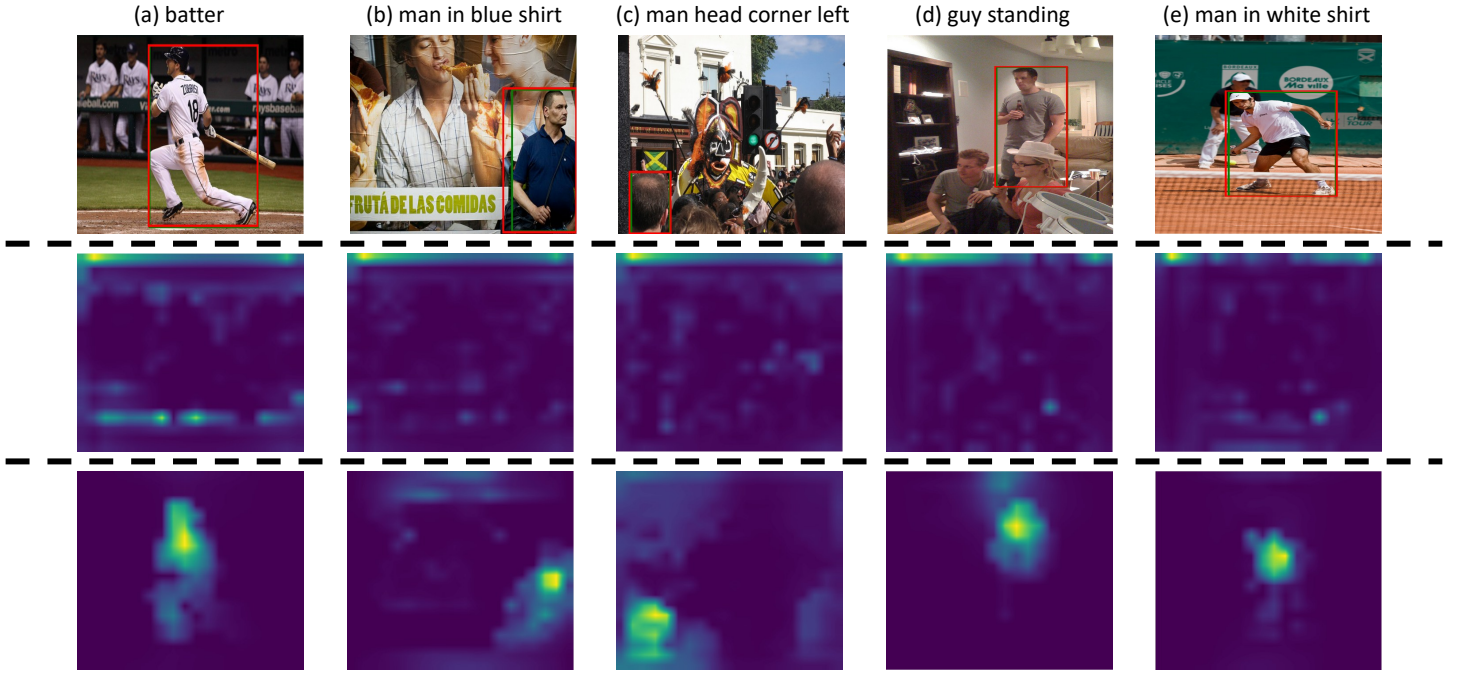


Figure 7: presents a comparative visualization of attention maps between the final attention layer before the Visual Discriminative Feature Encoder (middle row), and the final attention layer of the Visual Discriminative Feature Encoder (bottom row). The corresponding input image with prediction results and textual expressions are displayed in the top row. Red: prediction result; Green: ground truth.

vironmental elements for the localization task. For instance, in Fig. 7(d),(e), the Visual Discriminative Feature Encoder effectively highlights the approximate locations of target objects (i.e. "guy", "man") while suppressing irrelevant background information (e.g. "bookshelf", "billboard"), establishing a robust foundation for subsequent modules to further refine both the size and contours of these objects.

5. Conclusion

We propose PAML, a novel framework for open-vocabulary visual grounding that enhances cross-modal alignment, prototype-based reasoning, and deep multimodal fusion. By integrating ALBEF for robust feature encoding, a Visual Discriminative Feature Encoder for salient object enhancement, Multiple Neighbor Prototype Discovering and Inheriting for generalizable prototype learning and retrieval, and a Multi-Stage Decoder for thorough cross-modal integration, PAML achieves state-of-the-art performance in both standard and open-vocabulary scenes. Extensive experiments on five benchmarks validate its superiority, particularly in handling unseen objects and complex queries.

Future improvements could focus on several aspects to enhance model performance. The current framework employs ALBEF for data encoding, which could be replaced by more advanced vision-language models as they emerge to achieve better performance. Additionally, the prototype bank uses a fixed number of predefined prototypes, whereas adopting a dynamic mechanism to adjust the prototype count based on training data characteristics may yield more adaptive representations. Furthermore, the Transformer-based approach relies solely on REG tokens for bounding box regression, raising questions about whether this design enables sufficient fusion with multimodal features. Future work could explore alternative regression strategies to improve localization accuracy while maintaining effective multimodal integration.

CRedit authorship contribution statement

Jiangnan Xie: Methodology, Validation, Data curation, Formal analysis, Investigation, Writing - original draft. **Xiaolong Zheng:** Methodology, Investigation, Formal analysis, Supervision, Visualization, Writing - original draft, Writing - review & editing. **Liang Zheng:** Investigation, Formal analysis.

Declaration of competing interest

The authors declare that they have no known competing financial interests or personal relationships that could have appeared to influence the work reported in this paper.

Data availability

The datasets employed in this study were obtained from publicly available repositories, accessible via their corresponding references. The code used in this study is available at <https://github.com/plankXie/PAML>.

Acknowledgements

This work was supported by the National Key R&D Program of China (Grant No. 2024YFB4207200).

References

- [1] Peter Anderson, Qi Wu, Damien Teney, Jake Bruce, Mark Johnson, Niko Sünderhauf, Ian Reid, Stephen Gould, and Anton Van Den Hengel. Vision-and-language navigation: Interpreting visually-grounded navigation instructions in real environments. In *Proceedings of the IEEE conference on computer vision and pattern recognition*, pages 3674–3683, 2018. 1
- [2] Stanislaw Antol, Aishwarya Agrawal, Jiasen Lu, Margaret Mitchell, Dhruv Batra, C Lawrence Zitnick, and Devi Parikh. Vqa: Visual question answering. In *ICCV*, pages 2425–2433, 2015. 1
- [3] Hangbo Bao, Wenhui Wang, Li Dong, Qiang Liu, Owais Khan Mohammed, Kriti Aggarwal, Subhojit Som, Songhao Piao, and Furu Wei. Vlmo: Unified vision-language pre-training with mixture-of-modality-experts. *Advances in Neural Information Processing Systems*, 35:32897–32912, 2022. 1

- [4] Mikhail Belkin and Partha Niyogi. Semi-supervised learning on riemannian manifolds. *Machine learning*, 56:209–239, 2004. 5
- [5] Kan Chen, Jiyang Gao, and Ram Nevatia. Knowledge aided consistency for weakly supervised phrase grounding. In *Proceedings of the IEEE conference on computer vision and pattern recognition*, pages 4042–4050, 2018. 1
- [6] Long Chen, Wenbo Ma, Jun Xiao, Hanwang Zhang, and Shih-Fu Chang. Ref-nms: Breaking proposal bottlenecks in two-stage referring expression grounding. In *Proceedings of the AAAI conference on artificial intelligence*, volume 35, pages 1036–1044, 2021. 7
- [7] Long Chen, Xin Yan, Jun Xiao, Hanwang Zhang, Shiliang Pu, and Yueting Zhuang. Counterfactual samples synthesizing for robust visual question answering. In *CVPR*, pages 10800–10809, 2020. 1
- [8] Xinpeng Chen, Lin Ma, Jingyuan Chen, Zequn Jie, Wei Liu, and Jiebo Luo. Real-time referring expression comprehension by single-stage grounding network. *arXiv preprint arXiv:1812.03426*, 2018. 2, 7, 8
- [9] Zhuo Chen, Jiaoyan Chen, Yuxia Geng, Jeff Z Pan, Zonggang Yuan, and Huajun Chen. Zero-shot visual question answering using knowledge graph. In *The Semantic Web—ISWC 2021: 20th International Semantic Web Conference, ISWC 2021, Virtual Event, October 24–28, 2021, Proceedings 20*, pages 146–162. Springer, 2021. 1
- [10] Ming Dai, Jian Li, Jiedong Zhuang, Xian Zhang, and Wankou Yang. Multi-task visual grounding with coarse-to-fine consistency constraints. *Proceedings of the AAAI Conference on Artificial Intelligence*, 39(3):2618–2626, Apr. 2025. 2
- [11] Ming Dai, Lingfeng Yang, Yihao Xu, Zhenhua Feng, and Wankou Yang. Simvg: A simple framework for visual grounding with decoupled multi-modal fusion. *Advances in neural information processing systems*, 37:121670–121698, 2024. 2
- [12] Samyak Datta, Karan Sikka, Anirban Roy, Karuna Ahuja, Devi Parikh, and Ajay Divakaran. Align2ground: Weakly supervised phrase grounding guided by image-caption alignment. In *Proceedings of the IEEE/CVF international conference on computer vision*, pages 2601–2610, 2019. 1
- [13] Arthur P Dempster, Nan M Laird, and Donald B Rubin. Maximum likelihood from incomplete data via the em algorithm. *Journal of the royal statistical society: series B (methodological)*, 39(1):1–22, 1977. 6
- [14] Chaorui Deng, Qi Wu, Qingyao Wu, Fuyuan Hu, Fan Lyu, and Minghui Tan. Visual grounding via accumulated attention. In *Proceedings of the IEEE conference on computer vision and pattern recognition*, pages 7746–7755, 2018. 7
- [15] Jiajun Deng, Zhengyuan Yang, Tianlang Chen, Wengang Zhou, and Houqiang Li. Transvg: End-to-end visual grounding with transformers. In *Proceedings of the IEEE/CVF International Conference on Computer Vision*, pages 1769–1779, 2021. 2, 5, 6, 7, 8, 9, 10
- [16] Jiajun Deng, Zhengyuan Yang, Daqing Liu, Tianlang Chen, Wengang Zhou, Yanyong Zhang, Houqiang Li, and Wanli Ouyang. Transvg++: End-to-end visual grounding with language conditioned vision transformer. *IEEE transactions on pattern analysis and machine intelligence*, 45(11):13636–13652, 2023. 7, 8
- [17] Danny Driess, Fei Xia, Mehdi SM Sajjadi, Corey Lynch, Aakanksha Chowdhery, Ayzaan Wahid, Jonathan Tompson, Quan Vuong, Tianhe Yu, Wenlong Huang, et al. Palm-e: An embodied multimodal language model. 2023. 1
- [18] Ye Du, Zehua Fu, Qingjie Liu, and Yunhong Wang. Visual grounding with transformers. In *Proceedings of the International Conference on Multimedia and Expo*, 2022. 7, 8, 9, 10
- [19] Hugo Jair Escalante, Carlos A Hernández, Jesus A Gonzalez, Aurelio López-López, Manuel Montes, Eduardo F Morales, L Enrique Sucar, Luis Villaseñor, and Michael Grubinger. The segmented and annotated iapr tc-12 benchmark. *CVIU*, 114:419–428, 2010. 6
- [20] Xiuye Gu, Tsung-Yi Lin, Weicheng Kuo, and Yin Cui. Open-vocabulary object detection via vision and language knowledge distillation. In *International Conference on Learning Representations*, 2022. 1
- [21] Ruozhen He, Paola Cascante-Bonilla, Ziyang Yang, Alexander C Berg, and Vicente Ordonez. Improved visual grounding through self-consistent explanations. In *Proceedings of the IEEE/CVF Conference on Computer Vision and Pattern Recognition*, pages 13095–13105, 2024. 1
- [22] Richang Hong, Daqing Liu, Xiaoyu Mo, Xiangnan He, and Hanwang Zhang. Learning to compose and reason with language tree structures for visual grounding. *TPAMI*, 2019. 2, 7
- [23] Ronghang Hu, Marcus Rohrbach, Jacob Andreas, Trevor Darrell, and Kate Saenko. Modeling relationships in referential expressions with compositional modular networks. In *CVPR*, pages 1115–1124, 2017. 2, 7, 8
- [24] Ronghang Hu, Huazhe Xu, Marcus Rohrbach, Jiashi Feng, Kate Saenko, and Trevor Darrell. Natural language object retrieval. In *CVPR*, pages 4555–4564, 2016. 1
- [25] Xiaowei Hu, Xi Yin, Kevin Lin, Lei Zhang, Jianfeng Gao, Lijuan Wang, and Zicheng Liu. Vivo: Visual vocabulary pre-training for novel object captioning. In *proceedings of the AAAI conference on artificial intelligence*, volume 35, pages 1575–1583, 2021. 1
- [26] Binbin Huang, Dongze Lian, Weixin Luo, and Shenghua Gao. Look before you leap: Learning landmark features for one-stage visual grounding. In *Proceedings of the IEEE/CVF conference on computer vision and pattern recognition*, pages 16888–16897, 2021. 7, 8, 9
- [27] Pingping Huang, Jianhui Huang, Yuqing Guo, Min Qiao, and Yong Zhu. Multi-grained attention with object-level grounding for visual question answering. In *Proceedings of the 57th Annual Meeting of the Association for Computational Linguistics*, pages 3595–3600, 2019. 1
- [28] Haojun Jiang, Yuanze Lin, Dongchen Han, Shiji Song, and Gao Huang. Pseudo-q: Generating pseudo language queries for visual grounding. In *Proceedings of the IEEE/CVF Conference on Computer Vision and Pattern Recognition*, pages 15513–15523, 2022. 1, 6, 7, 8
- [29] Jianglin Jin, Jiabo Ye, Xin Lin, and Liang He. Pseudo-query generation for semi-supervised visual grounding with knowledge distillation. In *ICASSP 2023-2023 IEEE International Conference on Acoustics, Speech and Signal Processing (ICASSP)*, pages 1–5. IEEE, 2023. 1
- [30] Sahar Kazemzadeh, Vicente Ordonez, Mark Matten, and Tamara Berg. Referitgame: Referring to objects in photographs of natural scenes. In *EMNLP*, 2014. 6, 8
- [31] Rama Kovvuri and Ram Nevatia. Pirc net: Using proposal indexing, relationships and context for phrase grounding. In *ACCV*, pages 451–467, 2018. 7, 8
- [32] Aoxue Li, Zhiwu Lu, Jiechao Guan, Tao Xiang, Liwei Wang, and Ji-Rong Wen. Transferrable feature and projection learning with class hierarchy for zero-shot learning. *International Journal of Computer Vision*, 128:2810–2827, 2020. 1
- [33] Junnan Li, Dongxu Li, Caiming Xiong, and Steven Hoi. Blip: Bootstrapping language-image pre-training for unified vision-language understanding and generation. In *International conference on machine learning*, pages 12888–12900. PMLR, 2022. 1
- [34] Junnan Li, Ramprasaath Selvaraju, Akhilesh Gotmare, Shafiq Joty, Caiming Xiong, and Steven Chu Hong Hoi. Align before fuse: Vision and language representation learning with momentum distillation. *Advances in neural information processing systems*, 34:9694–9705, 2021. 1
- [35] Muchen Li and Leonid Sigal. Referring transformer: A one-step approach to multi-task visual grounding. *Advances in neural information processing systems*, 34:19652–19664, 2021. 6, 7, 8, 9, 10
- [36] Xiujun Li, Xi Yin, Chunyuan Li, Pengchuan Zhang, Xiaowei Hu, Lei Zhang, Lijuan Wang, Houdong Hu, Li Dong, Furu Wei, et al. Oscar: Object-semantics aligned pre-training for vision-language tasks. In *ECCV*, pages 121–137, 2020. 1
- [37] Yikang Li, Nan Duan, Bolei Zhou, Xiao Chu, Wanli Ouyang, Xiaogang Wang, and Ming Zhou. Visual question generation as dual task of visual question answering. In *Proceedings of the IEEE conference on computer vision and pattern recognition*, pages 6116–6124, 2018. 1

- [38] Yue Liao, Si Liu, Guanbin Li, Fei Wang, Yanjie Chen, Chen Qian, and Bo Li. A real-time cross-modality correlation filtering method for referring expression comprehension. In *CVPR*, pages 10880–10889, 2020. [2](#), [7](#), [8](#)
- [39] Yue Liao, Aixi Zhang, Zhiyuan Chen, Tianrui Hui, and Si Liu. Progressive language-customized visual feature learning for one-stage visual grounding. *IEEE Transactions on Image Processing*, 31:4266–4277, 2022. [2](#)
- [40] Tsung-Yi Lin, Michael Maire, Serge Belongie, James Hays, Pietro Perona, Deva Ramanan, Piotr Dollár, and C Lawrence Zitnick. Microsoft coco: Common objects in context. In *ECCV*, pages 740–755, 2014. [6](#)
- [41] Daqing Liu, Hanwang Zhang, Feng Wu, and Zheng-Jun Zha. Learning to assemble neural module tree networks for visual grounding. In *ICCV*, pages 4673–4682, 2019. [7](#)
- [42] Junhua Mao, Jonathan Huang, Alexander Toshev, Oana Camburu, Alan L Yuille, and Kevin Murphy. Generation and comprehension of unambiguous object descriptions. In *CVPR*, pages 11–20, 2016. [1](#), [6](#), [7](#)
- [43] Peihan Miao, Wei Su, Gaoang Wang, Xuewei Li, and Li Xi. Self-paced multi-grained cross-modal interaction modeling for referring expression comprehension. *IEEE Transactions on Image Processing*, 33:1497–1507, 2023. [7](#), [8](#)
- [44] Varun K Nagaraja, Vlad I Morariu, and Larry S Davis. Modeling context between objects for referring expression understanding. In *ECCV*, pages 792–807, 2016. [6](#)
- [45] Bryan A. Plummer, Paige Kordas, M. Hadi Kiapour, Shuai Zheng, Robinson Piramuthu, and Svetlana Lazebnik. Conditional image-text embedding networks. In *ECCV*, pages 249–264, 2018. [7](#), [8](#)
- [46] Bryan A Plummer, Liwei Wang, Chris M Cervantes, Juan C Caicedo, Julia Hockenmaier, and Svetlana Lazebnik. Flickr30k entities: Collecting region-to-phrase correspondences for richer image-to-sentence models. *IJCV*, 123(1):74, 2017. [6](#), [8](#)
- [47] Yuankai Qi, Qi Wu, Peter Anderson, Xin Wang, William Yang Wang, Chunhua Shen, and Anton van den Hengel. Reverie: Remote embodied visual referring expression in real indoor environments. In *Proceedings of the IEEE/CVF Conference on Computer Vision and Pattern Recognition*, pages 9982–9991, 2020. [1](#)
- [48] Rui Qian, Yeqing Li, Zheng Xu, Ming-Hsuan Yang, Serge Belongie, and Yin Cui. Multimodal open-vocabulary video classification via vision and language models, 2023. [1](#)
- [49] Alec Radford, Jong Wook Kim, Chris Hallacy, Aditya Ramesh, Gabriel Goh, Sandhini Agarwal, Girish Sastry, Amanda Askell, Pamela Mishkin, Jack Clark, et al. Learning transferable visual models from natural language supervision. In *International conference on machine learning*, pages 8748–8763. PMLR, 2021. [1](#)
- [50] David Rozenberszki, Or Litany, and Angela Dai. Language-grounded indoor 3d semantic segmentation in the wild. In *European Conference on Computer Vision*, pages 125–141. Springer, 2022. [1](#)
- [51] Arka Sadhu, Kan Chen, and Ram Nevatia. Zero-shot grounding of objects from natural language queries. In *ICCV*, pages 4694–4703, 2019. [2](#), [7](#), [8](#)
- [52] Haozhan Shen, Tiancheng Zhao, Mingwei Zhu, and Jianwei Yin. Groundvlp: Harnessing zero-shot visual grounding from vision-language pre-training and open-vocabulary object detection. In *Proceedings of the AAAI Conference on Artificial Intelligence*, volume 38, pages 4766–4775, 2024. [2](#)
- [53] Hengcan Shi, Munawar Hayat, and Jianfei Cai. Unpaired referring expression grounding via bidirectional cross-modal matching. *Neurocomputing*, 518:39–49, 2023. [1](#)
- [54] Zhan Shi, Yilin Shen, Hongxia Jin, and Xiaodan Zhu. Improving zero-shot phrase grounding via reasoning on external knowledge and spatial relations. In *Proceedings of the AAAI Conference on Artificial Intelligence*, volume 36, pages 2253–2261, 2022. [2](#)
- [55] Wei Su, Peihan Miao, Huanzhang Dou, and Xi Li. Scanformer: Referring expression comprehension by iteratively scanning. In *Proceedings of the IEEE/CVF Conference on Computer Vision and Pattern Recognition*, pages 13449–13458, 2024. [7](#), [8](#)
- [56] Wei Su, Peihan Miao, Huanzhang Dou, Gaoang Wang, Liang Qiao, Zheyang Li, and Xi Li. Language adaptive weight generation for multi-task visual grounding. In *Proceedings of the IEEE/CVF conference on computer vision and pattern recognition*, pages 10857–10866, 2023. [2](#)
- [57] Sanjay Subramanian, Will Merrill, Trevor Darrell, Matt Gardner, Sameer Singh, and Anna Rohrbach. Reclip: A strong zero-shot baseline for referring expression comprehension. In *Proceedings of the 60th Annual Meeting of the Association for Computational Linguistics*, Dublin, Ireland, may 2022. Association for Computational Linguistics. [2](#)
- [58] Jiamu Sun, Gen Luo, Yiyi Zhou, Xiaoshuai Sun, Guannan Jiang, Zhiyu Wang, and Rongrong Ji. Refteacher: A strong baseline for semi-supervised referring expression comprehension. In *Proceedings of the IEEE/CVF conference on computer vision and pattern recognition*, pages 19144–19154, 2023. [1](#)
- [59] Mingjie Sun, Jimin Xiao, Eng Gee Lim, and Yao Zhao. Cycle-free weakly referring expression grounding with self-paced learning. *IEEE Transactions on Multimedia*, 25:1611–1621, 2021. [1](#)
- [60] Hao Tang, Zechao Li, Zhimao Peng, and Jinhui Tang. Blockmix: meta regularization and self-calibrated inference for metric-based meta-learning. In *Proceedings of the 28th ACM international conference on multimedia*, pages 610–618, 2020. [1](#)
- [61] Hao Tang, Chengcheng Yuan, Zechao Li, and Jinhui Tang. Learning attention-guided pyramidal features for few-shot fine-grained recognition. *Pattern Recognition*, 130:108792, 2022. [1](#)
- [62] Wei Tang, Liang Li, Xuejing Liu, Lu Jin, Jinhui Tang, and Zechao Li. Context disentangling and prototype inheriting for robust visual grounding. *IEEE Transactions on Pattern Analysis and Machine Intelligence*, 46(5):3213–3229, 2023. [1](#), [2](#), [4](#), [5](#), [7](#), [8](#), [9](#), [10](#)
- [63] Ashish Vaswani, Noam Shazeer, Niki Parmar, Jakob Uszkoreit, Llion Jones, Aidan N Gomez, Lukasz Kaiser, and Illia Polosukhin. Attention is all you need. In *NeurIPS*, 2017. [2](#), [17](#)
- [64] Josiah Wang and Lucia Specia. Phrase localization without paired training examples. In *Proceedings of the IEEE/CVF International Conference on Computer Vision*, pages 4663–4672, 2019. [1](#)
- [65] Liwei Wang, Jing Huang, Yin Li, Kun Xu, Zhengyuan Yang, and Dong Yu. Improving weakly supervised visual grounding by contrastive knowledge distillation. In *Proceedings of the IEEE/CVF conference on computer vision and pattern recognition*, pages 14090–14100, 2021. [1](#)
- [66] Liwei Wang, Yin Li, Jing Huang, and Svetlana Lazebnik. Learning two-branch neural networks for image-text matching tasks. *TPAMI*, 41:394–407, 2018. [2](#), [7](#), [8](#)
- [67] Peng Wang, Qi Wu, Jiewei Cao, Chunhua Shen, Lianli Gao, and Anton van den Hengel. Neighbourhood watch: Referring expression comprehension via language-guided graph attention networks. In *CVPR*, pages 1960–1968, 2019. [7](#)
- [68] Peng Wang, An Yang, Rui Men, Junyang Lin, Shuai Bai, Zhikang Li, Jianxin Ma, Chang Zhou, Jingren Zhou, and Hongxia Yang. Ofa: Unifying architectures, tasks, and modalities through a simple sequence-to-sequence learning framework. In *International conference on machine learning*, pages 23318–23340. PMLR, 2022. [2](#)
- [69] Wenhui Wang, Hangbo Bao, Li Dong, Johan Bjorck, Zhiliang Peng, Qiang Liu, Kriti Aggarwal, Owais Khan Mohammed, Saksham Singhal, Subhojit Som, et al. Image as a foreign language: Beit pretraining for vision and vision-language tasks. In *Proceedings of the IEEE/CVF Conference on Computer Vision and Pattern Recognition*, pages 19175–19186, 2023. [1](#)
- [70] Yuechen Wang, Jiajun Deng, Wengang Zhou, and Houqiang Li. Weakly supervised temporal adjacent network for language grounding. *IEEE Transactions on Multimedia*, 24:3276–3286, 2021. [1](#)
- [71] Linhui Xiao, Xiaoshan Yang, Fang Peng, Yaowei Wang, and Changsheng Xu. Hivg: Hierarchical multimodal fine-grained modulation for visual grounding. In *Proceedings of the 32nd ACM International Conference on Multimedia*, pages 5460–5469, 2024. [2](#)
- [72] Linhui Xiao, Xiaoshan Yang, Fang Peng, Ming Yan, Yaowei Wang, and Changsheng Xu. Clip-vg: Self-paced curriculum adapting

- of clip for visual grounding. *IEEE Transactions on Multimedia*, 26:4334–4347, 2023. 1, 2, 7, 8
- [73] Wenjia Xu, Yongqin Xian, Juniu Wang, Bernt Schiele, and Zeynep Akata. Attribute prototype network for zero-shot learning. *Advances in Neural Information Processing Systems*, 33:21969–21980, 2020. 1
- [74] Dejie Yang, Zhu Xu, Wentao Mo, Qingchao Chen, Siyuan Huang, and Yang Liu. 3d vision and language pretraining with large-scale synthetic data. In *Proceedings of the Thirty-Third International Joint Conference on Artificial Intelligence, IJCAI '24*, 2024. 1
- [75] Li Yang, Yan Xu, Chunfeng Yuan, Wei Liu, Bing Li, and Weiming Hu. Improving visual grounding with visual-linguistic verification and iterative reasoning. In *Proceedings of the IEEE/CVF Conference on Computer Vision and Pattern Recognition*, pages 9499–9508, 2022. 7, 8, 9, 10
- [76] Sibe Yang, Guanbin Li, and Yizhou Yu. Dynamic graph attention for referring expression comprehension. In *ICCV*, pages 4644–4653, 2019. 2, 7
- [77] Zhengyuan Yang, Tianlang Chen, Liwei Wang, and Jiebo Luo. Improving one-stage visual grounding by recursive sub-query construction. In *ECCV*, 2020. 1, 2, 7, 8
- [78] Zhengyuan Yang, Boqing Gong, Liwei Wang, Wenbing Huang, Dong Yu, and Jiebo Luo. A fast and accurate one-stage approach to visual grounding. In *ICCV*, pages 4683–4693, 2019. 2, 7, 8
- [79] Yuan Yao, Ao Zhang, Zhengyan Zhang, Zhiyuan Liu, Tat-Seng Chua, and Maosong Sun. Cpt: Colorful prompt tuning for pre-trained vision-language models. *AI Open*, 5:30–38, 2024. 2
- [80] Raymond A Yeh, Minh N Do, and Alexander G Schwing. Un-supervised textual grounding: Linking words to image concepts. In *Proceedings of the IEEE Conference on Computer Vision and Pattern Recognition*, pages 6125–6134, 2018. 1
- [81] Peter Young, Alice Lai, Micah Hodosh, and Julia Hockenmaier. From image descriptions to visual denotations: New similarity metrics for semantic inference over event descriptions. *ACL*, 2:67–78, 2014. 6
- [82] Jiahui Yu, Zirui Wang, Vijay Vasudevan, Legg Yeung, Mojtaba Seyedhosseini, and Yonghui Wu. Coca: Contrastive captioners are image-text foundation models. *Transactions on Machine Learning Research*, 2022. 1
- [83] Licheng Yu, Zhe Lin, Xiaohui Shen, Jimei Yang, Xin Lu, Mohit Bansal, and Tamara L Berg. Mattnet: Modular attention network for referring expression comprehension. In *CVPR*, pages 1307–1315, 2018. 2, 7, 8
- [84] Licheng Yu, Patrick Poirson, Shan Yang, Alexander C Berg, and Tamara L Berg. Modeling context in referring expressions. In *ECCV*, pages 69–85, 2016. 1, 6, 7
- [85] Licheng Yu, Hao Tan, Mohit Bansal, and Tamara L Berg. A joint speaker-listener-reinforcer model for referring expressions. In *CVPR*, pages 7282–7290, 2017. 1
- [86] Zhou Yu, Jun Yu, Chenchao Xiang, Zhou Zhao, Qi Tian, and Dacheng Tao. Rethinking diversified and discriminative proposal generation for visual grounding. In *IJCAI*, 2018. 7, 8
- [87] Zhaohuan Zhan, Liang Lin, and Guang Tan. Object-aware navigation for remote embodied visual referring expression. *Neurocomputing*, 515:68–78, 2023. 1
- [88] Hanwang Zhang, Yulei Niu, and Shih-Fu Chang. Grounding referring expressions in images by variational context. In *CVPR*, pages 4158–4166, 2018. 7, 8
- [89] Minghang Zheng, Jiahua Zhang, Qingchao Chen, Yuxin Peng, and Yang Liu. Resvg: Enhancing relation and semantic understanding in multiple instances for visual grounding. In *Proceedings of the 32nd ACM International Conference on Multimedia*, pages 1187–1196, 2024. 2, 7, 8, 9, 10
- [90] Chaoyang Zhu, Yiyi Zhou, Yunhang Shen, Gen Luo, Xingjia Pan, Mingbao Lin, Chao Chen, Liujuan Cao, Xiaoshuai Sun, and Rongrong Ji. Seqtr: A simple yet universal network for visual grounding. In *Computer Vision–ECCV 2022: 17th European Conference, Tel Aviv, Israel, October 23–27, 2022, Proceedings, Part XXXV*, pages 598–615. Springer, 2022. 7, 8, 9, 10

- [91] Haidong Zhu, Arka Sadhu, Zhaoheng Zheng, and Ram Nevatia. Utilizing every image object for semi-supervised phrase grounding. In *Proceedings of the IEEE/CVF Winter Conference on Applications of Computer Vision*, pages 2210–2219, 2021. 1
- [92] Bohan Zhuang, Qi Wu, Chunhua Shen, Ian Reid, and Anton van den Hengel. Parallel attention: A unified framework for visual object discovery through dialogs and queries. In *CVPR*, pages 4252–4261, 2018. 2, 7
- [93] Eric R Ziegel. The elements of statistical learning, 2003. 6

A. Preliminary

Before delving into the specifics of the PAML model, we will first provide a brief introduction to three distinct types of attention mechanisms [63].

A.1. Self-Attention Mechanism

Mechanism The Self-Attention mechanism is employed to capture relationships among elements within a single sequence. Given an input sequence $X = (x_1, x_2, \dots, x_n)$, where $x_i \in \mathbb{R}^d$, the computation of Self-Attention proceeds as follows:

$$Q = XW_Q, K = XW_K, V = XW_V \quad (21)$$

Here $W_Q, W_K, W_V \in \mathbb{R}^{d \times d_k}$

$$Attention(Q, K, V) = softmax(\frac{QK^T}{\sqrt{d_k}})V \quad (22)$$

In Eq. (22), $\frac{QK^T}{\sqrt{d_k}}$ represents the scaled dot-product attention, and d_k denotes the dimensionality of the key vectors. Multi-head self-attention mechanism is a variant of single-head self-attention mechanism. While it is structurally similar to Eq. (22) in form, each attention head can be regarded as learning relationships between elements in the sequence from different “perspectives.” This introduction enhances the model’s ability to generalize to unseen data. In the subsequent sections, we will use $MSA(\cdot)$ to denote the Multi-head Self-Attention mechanism operation.

A.2. Cross-Attention Mechanism

The Cross-Attention mechanism is designed to capture interactions between different sequences. Given two input sequences from distinct modalities. $X = (x_1, x_2, \dots, x_n)$ and $Y = (y_1, y_2, \dots, y_n)$, where $x_i \in \mathbb{R}^{d_x}$ and $y_j \in \mathbb{R}^{d_y}$, the computation of Cross-Attention proceeds as follows:

$$Q = XW_Q, K = YW_K, V = YW_V \quad (23)$$

Here, $W_Q \in \mathbb{R}^{d_x \times d_k}$, and $W_K, W_V \in \mathbb{R}^{d_y \times d_k}$

$$Cross-attention(Q, K, V) = softmax(\frac{QK^T}{\sqrt{d_k}})V \quad (24)$$

Similarly, we use $MCA(\cdot)$ to denote the Multi-head Cross-attention mechanism operation.

A.3. Attention mechanism+Relative Positional Encoding

This is an enhanced attention mechanism that combines attention mechanism with relative positional encoding, capable of simultaneously capturing both the semantic relationships and the relative positional relationships among elements in sequences. Given three different sequences, $X = (x_1, x_2, \dots, x_n)$, $Y = (y_1, y_2, \dots, y_n)$ and $Z = (z_1, z_2, \dots, z_n)$. where $x_i \in \mathbb{R}^{d_x}$, $y_j \in \mathbb{R}^{d_y}$ and $z_t \in \mathbb{R}^{d_z}$ the computation of Cross-Attention PRE proceeds as follows:

$$Q = XW_Q, K = YW_K, V = ZW_V \quad (25)$$

Here, $W_Q \in \mathbb{R}^{d_x \times d_k}$, $W_k \in \mathbb{R}^{d_y \times d_k}$ and $W_V \in \mathbb{R}^{d_z \times d_k}$

$$\text{AttentionRPE}(Q, K, V) = \text{softmax}\left(\frac{QK^T + R}{\sqrt{d_k}}\right)V \quad (26)$$

R represents the relative positional encoding, which is utilized to model the relative positional relationships between elements. The specific computation method is as follows:

Let us define the following quantities:

- Batch size B , number of attention heads h , embedding dimension dim , and image height and width dimension H, W
- Input mask $\mathbf{M} \in \{0, 1\}^{B \times HW}$ with $\mathbf{M}_{b,i} = \text{key_padding_mask}[b, i]$
- Image mask $\mathbf{I} \in \{0, 1\}^{B \times H \times W} = \neg \mathbf{M}$ (reshaped)
- Query matrix $\mathbf{Q} \in \mathbb{R}^{(B \cdot h) \times (dim/h) \times HW}$
- Key weight matrix $\mathbf{W}_k \in \mathbb{R}^{dim \times dim}$

First compute the cumulative positions along rows and columns:

$$\begin{aligned} \mathbf{yy}_{b,i,j} &= \sum_{k=1}^j \mathbf{I}_{b,i,k} \quad \forall b \in [1, B], i \in [1, H], j \in [1, H] \\ \mathbf{xx}_{b,i,j} &= \sum_{k=1}^i \mathbf{I}_{b,k,j} \quad \forall b \in [1, B], i \in [1, W], j \in [1, W] \end{aligned} \quad (27)$$

Flatten these to $\mathbf{yy}, \mathbf{xx} \in \mathbb{R}^{B \times HW}$, then compute relative position differences:

$$\begin{aligned} \Delta \mathbf{yy} &= \mathbf{yy}_{:, :, \text{None}} - \mathbf{yy}_{:, \text{None}, :} \in \mathbb{R}^{B \times HW \times HW} \\ \Delta \mathbf{xx} &= \mathbf{xx}_{:, :, \text{None}} - \mathbf{xx}_{:, \text{None}, :} \in \mathbb{R}^{B \times HW \times HW} \end{aligned} \quad (28)$$

Define position mbeddeing matrices (either learnable or fixed):

$$\begin{aligned} \mathbf{P}_y &\in \mathbb{R}^{y_range \times (dim/2)} \\ \mathbf{P}_x &\in \mathbb{R}^{x_range \times (dim/2)} \end{aligned} \quad (29)$$

Project through key weights:

$$\begin{aligned} \mathbf{K}_y &= \mathbf{P}_y \mathbf{W}_k[:, dim/2, :]^T \in \mathbb{R}^{y_range \times dim} \\ \mathbf{K}_x &= \mathbf{P}_x \mathbf{W}_k[dim/2 :, :]^T \in \mathbb{R}^{x_range \times dim} \end{aligned} \quad (30)$$

Reshape and prepare for multi-head attention:

$$\begin{aligned} \mathbf{K}'_y &\in \mathbb{R}^{(B \cdot h) \times (dim/h) \times y_range} \\ \mathbf{K}'_x &\in \mathbb{R}^{(B \cdot h) \times (dim/h) \times x_range} \end{aligned} \quad (31)$$

Compute raw attention scores:

$$\begin{aligned} \mathbf{A}_y^{raw} &= \mathbf{Q} \mathbf{K}'_y{}^T \in \mathbb{R}^{(B \cdot h) \times HW \times y_range} \\ \mathbf{A}_x^{raw} &= \mathbf{Q} \mathbf{K}'_x{}^T \in \mathbb{R}^{(B \cdot h) \times HW \times x_range} \end{aligned} \quad (32)$$

Reshape and compute position indices:

$$\begin{aligned} \mathbf{I}_{yy} &= \Delta \mathbf{yy}_{:, \text{None}, :} + \text{pos_index_offset} \in \mathbb{Z}^{B \times h \times HW \times HW} \\ \mathbf{I}_{xx} &= \Delta \mathbf{xx}_{:, \text{None}, :} + \text{pos_index_offset} \in \mathbb{Z}^{B \times h \times HW \times HW} \end{aligned} \quad (33)$$

Gather final position attention scores:

$$\begin{aligned} \mathbf{A}_y[b, h, i, j] &= \mathbf{A}_y^{raw}[b, h, i, \mathbf{I}_{yy}[b, h, i, j]] \\ \mathbf{A}_x[b, h, i, j] &= \mathbf{A}_x^{raw}[b, h, i, \mathbf{I}_{xx}[b, h, i, j]] \end{aligned} \quad (34)$$

Combine the position attention scores:

$$\mathbf{R} = (\mathbf{A}_y + \mathbf{A}_x) \in \mathbb{R}^{(B \cdot h) \times HW \times HW} \quad (35)$$